Journal of Applied Mechanics

Brief Notes

A Brief Note is a short paper that presents a specific solution of technical interest in mechanics but which does not necessarily contain new general methods or results. A Brief Note should not exceed 2500 words *or equivalent* (a typical one-column figure or table is equivalent to 250 words; a one line equation to 30 words). Brief Notes will be subject to the usual review procedures prior to publication. After approval such Notes will be published as soon as possible. The Notes should be submitted to the Editor of the JOURNAL OF APPLIED MECHANICS. Discussions on the Brief Notes should be addressed to the Editorial Department, ASME International, Three Park Avenue, New York, NY 10016-5990, or to the Editor of the JOURNAL OF APPLIED MECHANICS. Discussions on Brief Notes appearing in this issue will be accepted until two months after publication. Readers who need more time to prepare a Discussion should request an extension of the deadline from the Editorial Department.

Discontinuities in the Sensitivity Curves of Laminated Cylindrical Shells

Yiska Goldfeld
Research Scientist

Izhak Sheinman
Professor Faculty of Civil Engineering, Technion–Israel Institute of Technology, 32000 Haifa, Israel

The discontinuity in the sensitivity of laminated cylindrical shells is investigated via the initial post-buckling analysis. A general procedure for sensitivity, based on Koiter's parameters and using the Donnell and Sanders shell theories, is developed and used for parametric study of the discontinuity phenomenon. It was found that the discontinuity occurs at points of change of the circumferential wave number. [DOI: 10.1115/1.1748341]

Introduction

Shell-like structures are very sensitive to initial geometry imperfections. One of the main goals, in this field, is to find the various parameters that influence the shell's sensitivity, thereby improving the behavior of the whole structure.

In the present note the characteristic behavior of the imperfection sensitivity is investigated on the aid of Koiter's asymptotic theory, [1]. Koiter showed that the imperfection sensitivity of a structure is related to its initial post-buckling behavior, In other words, it is governed by the immediate slope at the bifurcation point: if the latter is negative, the real buckling load will be less than the theoretical one and the shell is sensitive. Accordingly, fewer parameters are needed for characterizing the sensitivity behavior.

Here, the sensitivity curves of an isotropic and laminated cylindrical shell are studied in terms of the circumferential wave number (CWN). It was found, [2,3], that discontinuities always occur at points where the CWN is changed, and in the present note these points are sought.

Contributed by the Applied Mechanics Division of THE AMERICAN SOCIETY OF MECHANICAL ENGINEERS for publication in the ASME JOURNAL OF APPLIED MECHANICS. Manuscript received by the ASME Applied Mechanics Division, August 12, 2002; final revision, October 25, 2003. Associate Editor: T. E. Triantifyllides.

Governing Equations

The governing equations are derived for the Donnell, [4], and Sanders, [5], kinematic relations, [6]. They are obtained via the variational principle for laminated cylindrical shell. Formulation of the two approaches is based on the displacement components in the axial (u), circumferential (v), and normal (w) directions.

The equilibrium equations read:

$$N_{xx,x}+\frac{N_{x\theta,\theta}}{R}=0$$

$$N_{x\theta,x}+\frac{N_{\theta\theta,\theta}}{R}+\delta\left[\frac{M_{\theta\theta,\theta}}{R^2}+\frac{M_{x\theta,x}}{R}+\frac{N_{\theta\theta}}{R^2}(w_{,\theta}-v)-\zeta\frac{N_{\theta\theta}}{R^2}(w_{,\theta}-v)+\frac{N_{x\theta}}{R}w_{,x}\right]=0$$

$$M_{xx,xx}+\frac{2M_{x\theta,x\theta}}{R}+\frac{M_{\theta\theta,\theta\theta}}{R^2}-\frac{N_{\theta\theta}}{R}+(N_{xx}w_{,x})_{,x}+\frac{(N_{\theta\theta}w_{,\theta})_{,\theta}}{R^2}+\frac{(N_{x\theta}w_{,x})_{,\theta}}{R}+\frac{(N_{x\theta}w_{,\theta})_{,x}}{R}-\delta\left[\frac{(N_{\theta\theta}v)_{,\theta}}{R^2}+\frac{(N_{x\theta}v)_{,x}}{R}\right]+q_{zz}=0 \tag{1}$$

with the following boundary conditions:

$$u \quad \text{or} \quad N_{xx}$$

$$v \quad \text{or} \quad N_{x\theta}+\delta\frac{M_{x\theta}}{R}$$

$$w \quad \text{or} \quad M_{xx,x}+\frac{2M_{x\theta,\theta}}{R}+N_{xx}w_{,x}+\frac{N_{x\theta}w_{,\theta}}{R}-\delta\frac{N_{x\theta}v}{R}$$

$$w_{,x} \quad \text{or} \quad M_{xx} \tag{2}$$

where
$\delta=0$ for Donnell's kinematic relations
$\delta=1$ for Sanders' kinematic relations.

ζ is a correction factor for the second theory ($\delta=1$) in the hydrostatic load case, [7,8]: $\zeta=0$ when the load remains parallel to its original, and $\zeta=1$ when the load remains normal to the deflected reference axis. The difference between the two versions is most pronounced for thin rings.

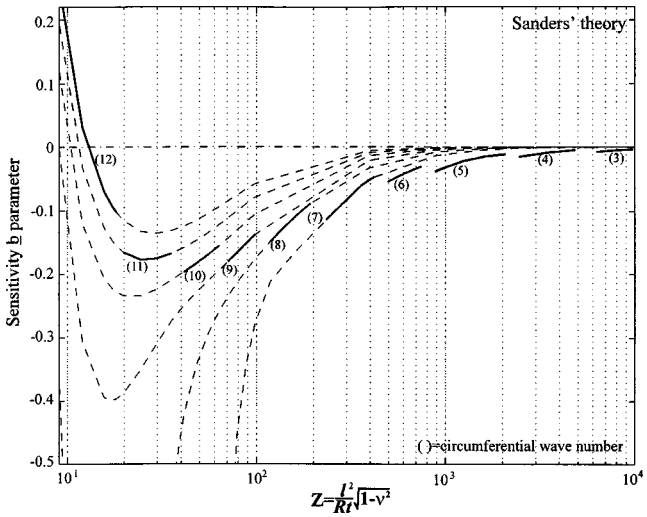

Fig. 1 Sensitivity b parameter versus Batdorf *Z*-parameter for simply supported ($N_{xx}=N_{x\theta}=0$) cylindrical shell under hydrostatic pressure

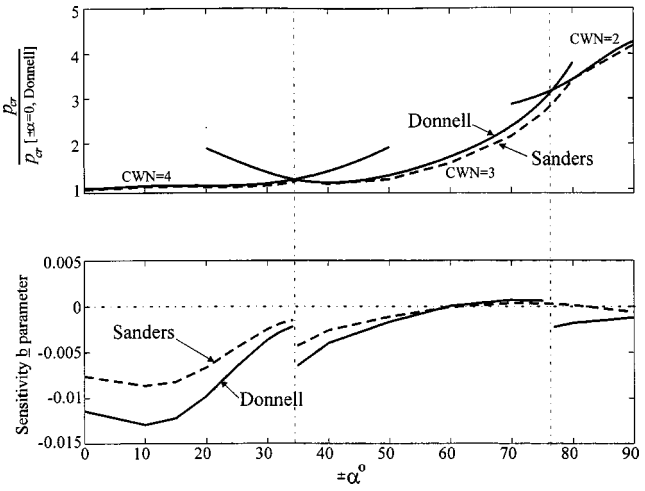

Fig. 3 Hydrostatic buckling load and sensitivity b parameter versus angle ply for simply supported ($N_{xx}=v=0$) cylindrical shell with $l/R=10$

Initial Post-buckling

The imperfection sensitivity parameters determine whether the load increases or decreases after buckling. Accordingly, the displacement, strain and stress vectors are expanded according to the following scheme:

$$\begin{Bmatrix} u \\ v \\ w \end{Bmatrix} = \lambda \begin{Bmatrix} u^{(0)} \\ v^{(0)} \\ w^{(0)} \end{Bmatrix} + \xi \begin{Bmatrix} u^{(1)} \\ v^{(1)} \\ w^{(1)} \end{Bmatrix} + \xi^2 \begin{Bmatrix} u^{(2)} \\ v^{(2)} \\ w^{(2)} \end{Bmatrix} + \ldots . \qquad (3)$$

The load parameter λ representing the deviation from the classical buckling load λ_c, and ξ being the perturbation parameter. The superscripts $^{(0)}$, $^{(1)}$ and $^{(2)}$ denote the prebuckling, buckling, and initial post-buckling states, respectively.

Applying the variational principle following Budiansky and Hutchinson, [9,10], the load parameter is obtained as

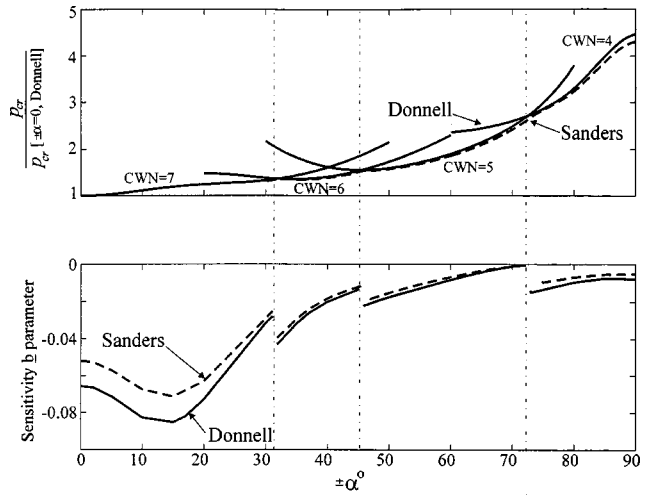

Fig. 2 Hydrostatic buckling load and sensitivity b parameter versus angle ply for simply supported ($N_{xx}=v=0$) cylindrical shell with $l/R=3$

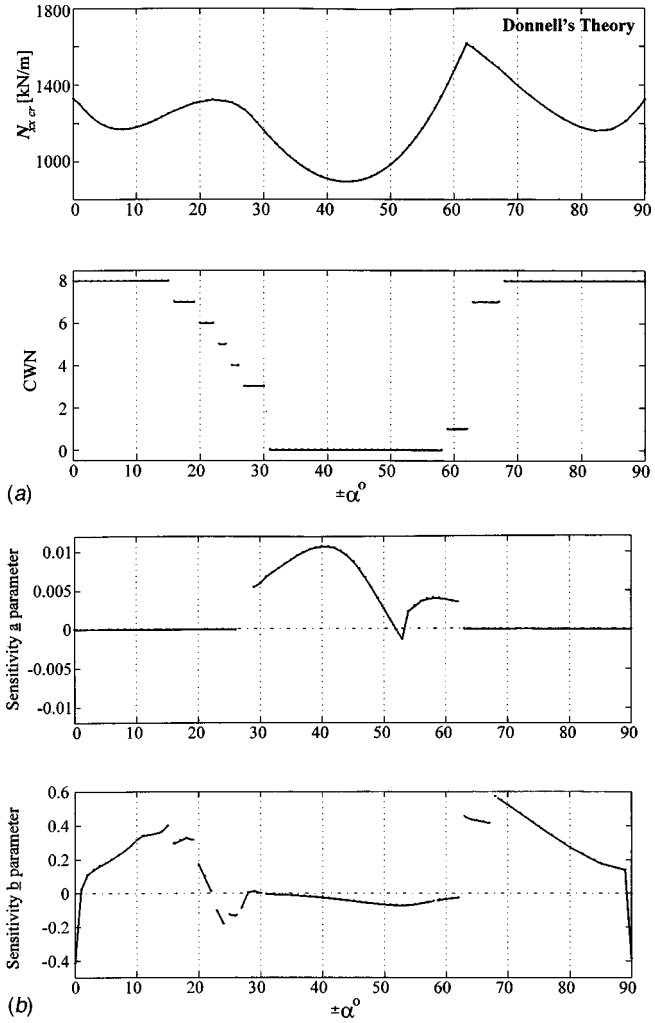

Fig. 4 (*a*) Axial buckling load and circumferential wave number versus angle ply for simply supported ($v=0$) cylindrical shell with $l/R=3$ (*b*) Sensitivity a and b parameters versus angle ply for simply supported ($v=0$) cylindrical shell with $l/R=3$

$$\frac{\lambda}{\lambda_c} = 1 + a\xi + b\xi^2 + \cdots \tag{4}$$

where a and b are known as the Koiter parameters. For isotropic cylindrical shells the coefficient a vanishes due to the periodicity of the buckling mode in the circumferential direction, but for a laminated cylindrical shell under axial compression it was found that it does not. As for the coefficient b a positive value indicates that the shell is insensitive, a negative value measures the level of sensitivity. For the linear prebuckling state Budiansky and Hutchinson derived the well-known formulas:

$$a = -\frac{3\sigma_1 \cdot L_2(u_1)}{2\lambda_c \sigma_0 \cdot L_2(u_1)} \tag{5}$$

$$b = -\frac{\sigma_2 \cdot L_2(u_1) + 2\sigma_1 \cdot L_{11}(u_1, u_2)}{\lambda_c \sigma_0 \cdot L_2(u_1)}. \tag{6}$$

In terms of the displacement components the operator is written as

$$\begin{aligned}\sigma_i \cdot L_{11}(u_j, u_k) = \int_a^b \int_0^{2\pi} \Bigg\{ & N_{xx}^{(i)}[w_{,x}^{(j)} w_{,x}^{(k)}] + N_{\theta\theta}^{(i)} \Bigg[\frac{w_{,\theta}^{(j)} w_{,\theta}^{(k)}}{R^2} \\ & - \frac{\delta}{R^2}(v^{(j)} w_{,\theta}^{(k)} + v^{(k)} w_{,\theta}^{(j)}) \Bigg] \\ & + 2N_{x\theta}^{(i)} \Bigg[\frac{w_{,x}^{(j)} w_{,\theta}^{(k)}}{2R} + \frac{w_{,x}^{(k)} w_{,\theta}^{(j)}}{2R} - \frac{\delta}{2R}(v^{(j)} w_{,x}^{(k)} \\ & + v^{(k)} w_{,x}^{(j)}) \Bigg] \Bigg\} d\theta dx \quad i,j,k \\ = 0,1,2 \end{aligned} \tag{7}$$

The superscripts (i), (j), and (k) denote the relevant state as above.

These equations are solved through expansion of the dependent variables in Fourier series in the circumferential direction and in finite differences in the axial direction. Afterwards the Galerkin procedure is used to minimize the error due to the truncated form of the series.

Parametric Study

In order to locate the discontinuities in the sensitivity curves, one must first find the critical CWN which yields the minimum buckling load; a change in the wave number causes a discontinuity in the slope of the buckling curve. After that, one must calculate Koiter's sensitivity parameters (Eqs. (5) and (6)), using the critical buckling load and its associated wave number, here again, the sensitivity curve is characterized by a discontinuity, but unlike the buckling curves the discontinuity occurs in the curve itself.

For this purpose isotropic cylindrical shells and laminated two-ply ($\pm\alpha$) angle-ply cylindrical shells under hydrostatic and axial loading are considered, reproduced from Sheinman and Goldfeld [6].

Hydrostatic Pressure. In the first case Budiansky and Amazigo's, [11], simply supported isotropic cylindrical shell was reproduced here. At their work there was no consideration to the varying CWN and the sensitivity curve was continuous. Here, see Fig. 1, it is seen that the b parameter is highly dependent on the CWN and acquires a discontinuity on a change in the latter. Thus not only the critical buckling load characterized by transaction of the CWN is dependent on the Batdorf Z-parameter, but the b parameter (Eq. 6) as well. It is worth noting that in this example Donnell's and Sanders' theories yield the same values.

In the second case (laminated cylindrical shell) the buckling load and the b are plotted against the angle-ply ($\pm\alpha$) in Figs. 2 and 3 for $l/R=3$ and 10, respectively. It is seen that both of them likewise highly dependent on the CWN, and the b parameter acquires a discontinuity as in the first case. It is found that the initial circumferential internal force, $N_{\theta\theta}$ affects it most.

Furthermore, it is seen that the buckling load and the sensitivity are also highly dependent on the angle ply. Regarding the sensitivity level, it is seen that the angle ply has the same effect as a stringer, namely, as it increases so does the buckling load while the sensitivity decreases.

The different between Sanders' and Donnell's shell theories is insignificant for buckling load but still Sanders' yield lower values, and quite pronounced for the b parameter; the more accurate the theory (Sanders), the lower the sensitivity and the buckling load.

Axial Compression. The axial buckling load (applied by setting $N_{xx}=\overline{N}_{xx}$ at one edge), the CWN, the a and b parameters are plotted againset the angle ply ($\pm\alpha$) in Fig. 4 according to Donnell's theory. Here, again, the discontinuities occur at points where the CWN changes, both in the b parameter and in the slope of the buckling-load curve (at $\pm\alpha=62°$ the transition is most pronounced, from CWN=1 to CWN=7).

Unlike its isotropic counter part, for the laminated cylindrical shell the a parameter does not necessarily vanish: for CWN=0 (axisymmetric buckling mode), the sensitivity is characterized by the asymmetric a parameter and while for CWN$\neq$0 it is characterized by the b parameter.

Conclusions

From the results the following conclusions can be drawn:

- Discontinuities in the b parameter always occur at points where the critical circumferential wave number changes.
- Where the sensitivity a parameter is not zero, the sensitivity b parameter vanishes, and vice versa.
- The angle ply has, in some cases, the same effect as a stringer configuration: as it increases does the buckling load, while the sensitivity decreases.

References

[1] Koiter, W. T., 1945, thesis, Delft, Amsterdam, H. J. Paris; Technical Report AFFDL-TR-70-25, Air Force Flight Dynamics Laboratory, Air Force Systems Command, Wright-Patterson Air Force Base, OH, Feb. 1970 (translated edition).

[2] Arbocz, J., and Hol, J. M. A. M., 1989, "ANILISA—Computational Modules for Koiter's Imperfection Sensitivity Theory," Report LR-582, Faculty of Aerospace Engineering, Delft University of Technology.

[3] Arbocz, J., and Hol, J. M. A. M., 1990, "Koiter's Stability Theory in a Computer-Aided Engineering (CAE) Environment," Int. J. Solids Struct., **26**(9/10), pp. 945–973.

[4] Donnell, L. H., 1933, "Stability of Thin-Walled Tubes Under Torsion," NACA TR-479.

[5] Sanders, J. L., 1963, "Nonlinear Theories for Thin Shells," Quar. J. Appl. Math., **21**(1), pp. 21–36.

[6] Sheinman, I., and Goldfeld, Y., 2001, "Buckling of Laminated Cylindrical Shells in Terms of Different Shell Theories and Formulations," AIAA J., **39**(9), pp. 1773–1781.

[7] Simitses, G. J., 1986, *An Introduction to the Elastic Stability of Structures*, Robert E. Krieger, Malabar, FL.

[8] Sheinman, I., and Tene, Y., 1973, "Potential Energy of a Normal Pressure Field Acting on an Arbitrary Shell," AIAA J., **11**(8), p. 1216.

[9] Budiansky, B., and Hutchinson, J. W., 1964, "Dynamic Buckling of Imperfection Sensitive Structures," *Proceedings XI International Congress on Applied Mechanics*, Munich, pp. 83–106.

[10] Hutchinson, J. W., and Budiansky, B., 1966, "Dynamic Buckling Estimates," AIAA J., **4**(3), pp. 525–530.

[11] Budiansky, B., and Amazigo, J. C., 1968, "Initial Post-buckling of Cylindrical Shells Under Hydrostatic Pressure," J. Math. Phys., **47**, pp. 223–235.

A Combined Fourier Series–Galerkin Method for the Analysis of Functionally Graded Beams

H. Zhu
Graduate Student

B. V. Sankar
Professor,
Fellow ASME

Department of Mechanical and Aerospace Engineering,
University of Florida, Gainesville, FL 32611-6250

The method of Fourier analysis is combined with the Galerkin method for solving the two-dimensional elasticity equations for a functionally graded beam subjected to transverse loads. The variation of the Young's modulus through the thickness is given by a polynomial in the thickness coordinate and the Poisson's ratio is assumed to be constant. The Fourier series method is used to reduce the partial differential equations to a pair of ordinary differential equations, which are solved using the Galerkin method. Results for bending stresses and transverse shear stresses in various beams show excellent agreement with available exact solutions. The method will be useful in analyzing functionally graded structures with arbitrary variation of properties.
[DOI: 10.1115/1.1751184]

Introduction

Functionally graded materials (FGMs) possess properties that vary gradually with location within the material. FGMs differ from composites wherein the volume fraction of the inclusion is uniform throughout the composite. The closest analogies of FGMs are laminated composites, but the latter possess distinct interfaces across which properties change abruptly. Suresh and Mortensen [1] provide an excellent introduction to the fundamentals of FGMs. As the use of FGMs increases, for example, in aerospace, automotive, and biomedical applications, new methodologies have to be developed to characterize FGMs, and also to design and analyze structural components made of these materials. For example, Pindera and Dunn [2] developed a higher order micromechanical theory for FGMs (HOTFGM) that explicitly couples the local and global effects. Delale and Erdogan [3] derived the crack-tip stress fields for an inhomogeneous cracked body with constant Poisson ratio and with a shear modulus variation given by $\mu = \mu_0 e^{(\alpha x + \beta y)}$. In general the analytical methods should be such that they can be incorporated into available methods with the least amount of modifications, if any. One such problem is that of response of FGMs to thermomechanical loads. Although FGMs are highly heterogeneous, it will be useful to idealize them as continua with properties changing smoothly with respect to the spatial coordinates. This will enable obtaining closed-form solutions to some fundamental solid mechanics problems, and also will help in developing finite element models of the structures made of FGMs.

In a series of papers Sankar and his co-workers, [4–7], reported analytical methods for the thermomechanical and contact analysis of FGM beams and also for sandwich beams with FG cores. In these studies the thermomechanical properties of the FGM were assumed to vary through the thickness in an exponential fashion, e.g., $E(z)=E_0 e^{\lambda z}$. The material was assumed to be isotropic at every point and the Poisson's ratio was assumed to be constant everywhere. This assumption enabled them to obtain analytical solutions using Fourier expansion methods. However, in practice the properties of FGM will vary in an arbitrary fashion and the aforementioned solution technique may not be useful. In the present paper we assume that the property variation through the thickness can be expressed in the form of a polynomial in the z coordinate. We demonstrate the application of both Fourier series and Galerkin methods for obtaining an approximate solution for displacements and stresses in a FG beam. The solutions are compared with available exact solutions and the agreement is found to be very good.

Contributed by the Applied Mechanics Division of THE AMERICAN SOCIETY OF MECHANICAL ENGINEERS for publication in the ASME JOURNAL OF APPLIED MECHANICS. Manuscript received by the ASME Applied Mechanics Division, July 1, 2002, final revision, December 5, 2003. Associate Editor: R. R. C. Benson.

Analysis

Consider a functionally graded (FG) beam of height h and length L as shown in Fig. 1. The beam and the loading are symmetric about the center line $x=L/2$. The beam is assumed to be in a state of plane strain normal to the x-z plane.

The transverse load $p_z(x)$ acting on the beam can be represented by a Fourier series as

$$\sigma_{zz}(x,0) = -p_z(x) = -p_n \sin \xi x \tag{1a}$$

where $\xi = n\pi/L$, $n=1,3,5\ldots$ and Fourier coefficients p_n are given by

$$p_n = \frac{2}{L}\int_0^L p_z(x)\sin \xi x dx. \tag{1b}$$

We will demonstrate the solution method for the load $p_n \sin \xi x$ in this note. Then the traction boundary condition on the bottom surface of the beam is given by

$$\sigma_{zz}(x,0) = -p_n \sin \xi x, \quad \tau_{xz}=0. \tag{1c}$$

Since n is odd, the load is also symmetric about the centerline. The boundary conditions are similar to that of a simply supported beam, but the actual boundary conditions will become clear later.

We assume that the FGM is isotropic at every point and the Poisson's ratio v is a constant through the thickness. The variation of Young's modulus E in the thickness direction is given by a polynomial in z as

$$E(z) = E_0\left(a_1 + a_2\left(\frac{z}{h}\right) + a_3\left(\frac{z}{h}\right)^2 + a_4\left(\frac{z}{h}\right)^3\right) \tag{2}$$

where E_0 is the Young's modulus at $z=0$, and a_1, a_2, a_3, and a_4 are material constants.

The differential equations of equilibrium are

$$\frac{\partial \sigma_{xx}}{\partial x} + \frac{\partial \tau_{xz}}{\partial z} = 0$$
$$\frac{\partial \tau_{xz}}{\partial x} + \frac{\partial \sigma_{zz}}{\partial z} = 0. \tag{3}$$

Assuming that the principal material directions coincide with the x and z-axes, the constitutive equations are

$$\begin{Bmatrix} \sigma_{xx} \\ \sigma_{zz} \\ \tau_{xz} \end{Bmatrix} = \begin{bmatrix} c_{11} & c_{13} & 0 \\ c_{13} & c_{33} & 0 \\ 0 & 0 & c_{55} \end{bmatrix} \begin{Bmatrix} \varepsilon_{xx} \\ \varepsilon_{zz} \\ \gamma_{xz} \end{Bmatrix} \tag{4}$$

or

$$\sigma = C\varepsilon.$$

The elasticity matrix $[C]$ is related to material constants by

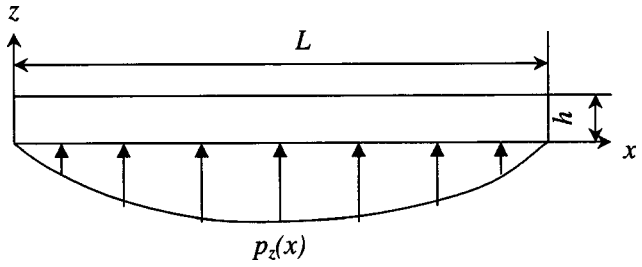

Fig. 1 A FGM beam subjected to symmetric transverse loading

$$C^{-1}=\begin{pmatrix} \frac{1}{E_{11}} & \frac{-\nu_{13}}{E_{11}} & 0 \\ \frac{-\nu_{13}}{E_{11}} & \frac{1}{E_{33}} & 0 \\ 0 & 0 & \frac{1}{G_{13}} \end{pmatrix}. \tag{5}$$

We assume the solution for displacements as

$$\begin{aligned} u(x,z)&=U(z)\cos\xi x \\ w(x,z)&=W(z)\sin\xi x \end{aligned} \tag{6}$$

Substituting Eq. (6) into (4), we obtain

$$\begin{pmatrix} \sigma_{xx} \\ \sigma_{zz} \\ \tau_{xz} \end{pmatrix}=\begin{pmatrix} c_{11} & c_{13} & 0 \\ c_{13} & c_{33} & 0 \\ 0 & 0 & G \end{pmatrix}\begin{pmatrix} -\xi U\sin\xi x \\ W'\sin\xi x \\ (U'+\xi W)\cos\xi x \end{pmatrix}. \tag{7}$$

The prime ($'$) after a variable denotes differentiation with respect to z. With Eqs. (6) and (7), one can state that the boundary conditions of the beam at $x=0$ and $x=L$ are $w(0,z)=w(L,z)=0$ and $\sigma_{xx}(0,z)=\sigma_{xx}(L,z)=0$, which corresponds to simply support conditions in the context of beam theory. Equations (7) can be written as

$$\begin{aligned} \begin{pmatrix} \sigma_{xx} \\ \sigma_{zz} \end{pmatrix}&=\begin{pmatrix} S_x \\ S_z \end{pmatrix}\sin\xi x \\ \tau_{xz}&=T_z\cos\xi x \end{aligned} \tag{8}$$

where

$$\begin{aligned} \begin{pmatrix} S_x \\ S_z \end{pmatrix}&=\begin{pmatrix} c_{11} & c_{13} \\ c_{13} & c_{33} \end{pmatrix}\begin{pmatrix} -\xi U \\ W' \end{pmatrix} \\ T_z&=G(U'+\xi W). \end{aligned} \tag{9}$$

Substituting for σ_{xx}, σ_{zz}, τ_{xz} from Eqs. (7) into equilibrium Eqs. (3), we obtain a set of ordinary differential equations in $U(z)$ and $W(z)$:

$$\begin{aligned} \xi S_x+T_z'&=0 \\ S_z'-T_z\xi&=0. \end{aligned} \tag{10}$$

In order to solve Eqs. (10) we employ the Galerkin method. We assume solutions of the form

$$\begin{aligned} U(z)&=c_1\phi_1(z)+c_2\phi_2(z)+c_3\phi_3(z)+c_4\phi_4(z) \\ W(z)&=b_1\phi_1(z)+b_2\phi_2(z)+b_3\phi_3(z)+b_4\phi_4(z) \end{aligned} \tag{11}$$

where ϕ_s are basis functions, and b_s and c_s are coefficients to be determined. For simplicity we choose 1, z, z^2, z^3 as basis functions. That is,

$$\phi_1(z)=1; \quad \phi_2(z)=z; \quad \phi_3(z)=z^2; \quad \phi_4(z)=z^3. \tag{12}$$

Substituting the approximate solution in the governing differential equations, we obtain the residuals. The residuals are minimized by equating their weighted averages to zero:

$$\begin{aligned} \int_0^h(\xi S_x+T_z')\phi_i(z)dz=0, \quad i=1,4 \\ \int_0^h(S_z'-T_z\xi)\phi_i(z)dz=0, \quad i=1,4. \end{aligned} \tag{13}$$

Using integration by parts we can rewrite Eqs. (13) as

$$\begin{aligned} &\int_0^h\phi_i\xi S_x dz+T_z(h)\phi_i(h)-T_z(0)\phi_i(0)-\int_0^h T_z\phi_i'dz=0 \\ &\qquad i=1,4 \\ &\int_0^h S_z\phi_i'dz+\int_0^h T_z\xi\phi_i dz-(S_z(h)\phi_i(h)-S_z(0)\phi_i(0))=0 \\ &\qquad i=1,4. \end{aligned} \tag{14}$$

Substituting for $S_x(z)$, $S_z(z)$, and $T_z(z)$ from Eqs. (9) into (14) and using the approximate solution for $U(z)$ and $W(z)$ in (11) we obtain

$$\begin{pmatrix} K_{ij}^{(1)} & K_{ij}^{(2)} \\ K_{ij}^{(3)} & K_{ij}^{(4)} \end{pmatrix}\begin{pmatrix} b \\ c \end{pmatrix}=\begin{pmatrix} f_i^{(1)} \\ f_i^{(2)} \end{pmatrix} \tag{15}$$

where

$$\begin{aligned} K_{ij}^{(1)}&=\xi\int_0^h c_{13}\phi_i\phi_j'dz-\xi\int_0^h G\phi_i'\phi_j dz \\ K_{ij}^{(2)}&=-\int_0^h G\phi_i'\phi_j'dz-\xi^2\int_0^h c_{11}\phi_i\phi_j dz \\ K_{ij}^{(3)}&=-\xi^2\int_0^h G\phi_i\phi_j dz-\int_0^h c_{33}\phi_i'\phi_j'dz \\ K_{ij}^{(4)}&=\xi\int_0^h c_{13}\phi_i'\phi_j dz-\xi\int_0^h G\phi_i\phi_j'dz \\ f_i^{(1)}&=\phi_i(0)T_z(0)-\phi_i(h)T_z(h) \\ f_i^{(2)}&=\phi_i(0)S_z(0)-\phi_i(h)S_z(h) \\ \begin{pmatrix} b \\ c \end{pmatrix}^T&=(b_1\ b_2\ b_3\ b_4\ c_1\ c_2\ c_3\ c_4). \end{aligned} \tag{16}$$

Traction boundary conditions on the top and bottom surfaces of beam are

$$\begin{aligned} \tau_{xz}(x,0)&=0 \\ \tau_{xz}(x,h)&=0 \\ \sigma_{zz}(x,0)&=-p_n\sin\xi x \\ \sigma_{zz}(x,h)&=0. \end{aligned} \tag{17}$$

In terms of S_z and T_z, the boundary conditions take the form

$$\begin{aligned} T_z(0)=T_z(h)&=0 \\ S_z(0)&=-p_n \\ S_z(h)&=0. \end{aligned} \tag{18}$$

Equations (18) can be used to evaluate $f_i^{(1)}$ and $f_i^{(2)}$ in (16) which are the right-hand side of Eq. (15). Solving Eq. (15), we obtain the solutions for the coefficients b_i and c_i, which yield the approximate solutions for $U(z)$ and $W(z)$ in (11). Once $U(z)$ and $W(z)$ are determined, stress at any point can be computed using Eqs. (8) and (9).

Table 1 The coefficients of the cubic polynomial for $E(z)$. $E_0 = 10$ GPa and beam thickness $h = 10$ mm.

E_h/E_0	a_1	a_2	a_3	a_4
10	1	2.9577	−0.7889	6.7982
0.1	1	−2.1845	1.9844	−0.6996

Results and Discussion

In order to verify the present method examples from [1] are used. In these examples the variation of Young's modulus is assumed to be of the form $E = E_0 e^{\lambda z/h}$. The same variation can be approximated by the polynomial form given in Eq. (2). The coefficients of the polynomial, $a_1, \ldots a_4$ were determined by using the least squares curve fitting. Two types of beams were considered, and the variation of Young's modulus in these beams are given by $E_h/E_0 = 10$ and $E_h/E_0 = 0.1$, respectively. In the first beam the load is applied on the softer face of the beam and in the second on the harder side. In both cases E_0 was taken as 1 GPa and $\nu = 0.25$. The thickness of the beam is $h = 10$ mm. The coefficients of the cubic polynomial for $E(z)$ are given in Table 1.

The results for the normalized bending stress for various values of $\xi h = n\pi/L$ are presented in Figs. 2 and 3. It should be noted that smaller values of ξh represent slender beams or beams subjected to more uniformly distributed loads, whereas larger values of ξh indicate short stubby beams or beams subjected to concentrated loads. From Figs. 2 and 3 it can be noted that the results of the Galerkin method agree very well with the exact solution, [1]. The difference of two solutions is imperceptible. The normalized stresses are less than 1 when the loads are applied to the softer face (Fig. 2, $E_h/E_0 = 10$). On the other hand, the normalized stresses are much greater than 1 when the loads are applied to the harder face (Fig. 3, $E_h/E_0 = 0.1$). One can also note the approximate location of the neutral axis for the two beams in these figures.

The transverse shear stresses are plotted in Figs. 4 and 5. The approximate solution also agrees well with exact solitions. The shear stresses attain the maximum value at the neutral axis. The normalized maximum shear stress values are above the conventional 1.5, when the loads are applied on the harder surface of the beam (Fig. 5), but fall below 1.5, in some cases when the loads are applied to the soft side (Fig. 4).

The present method can be applied to functionally graded structures with arbitrary variation of properties and also can be extended to platelike structures and sandwich construction wherein the core material and/or the face sheets are functionally graded.

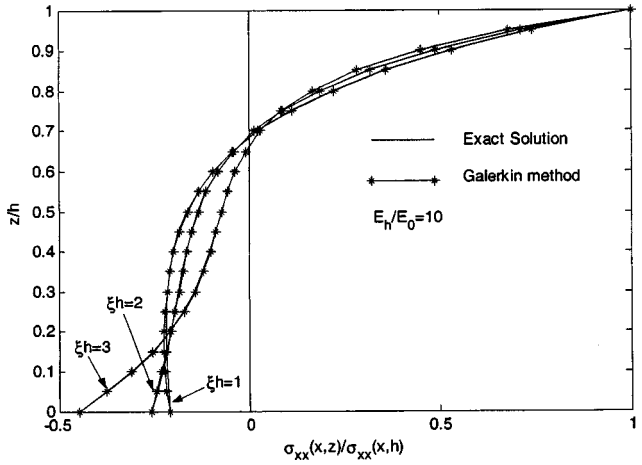

Fig. 2 Normalized axial stress σ_{xx} through the thickness of FGM beam for $E_h = 10\,E_0$. The exact solution and that of Galerkin method are indistinguishable.

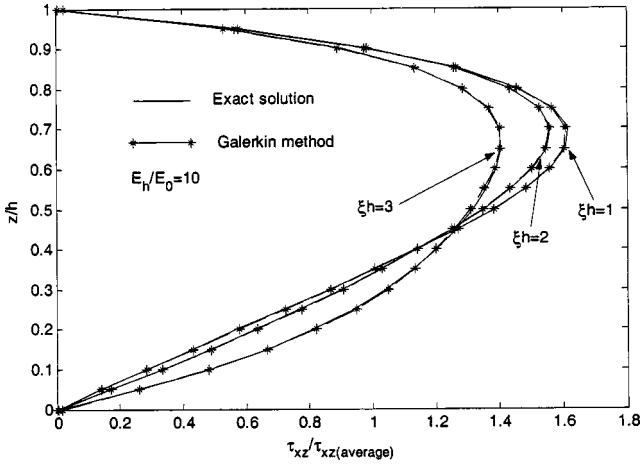

Fig. 4 Transverse shear stress through the thickness of FGM beam for $E_h = 10\,E_0$. The exact solution and that of Galerkin method are indistinguishable.

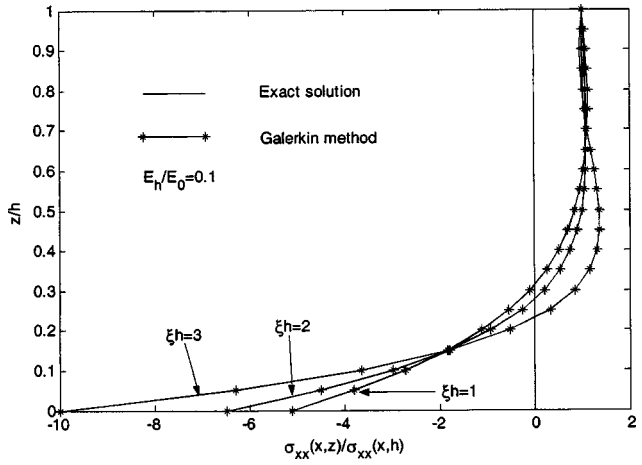

Fig. 3 Normalized axial stress σ_{xx} through the thickness of FGM beam for $E_h = 0.1\,E_0$. The exact solution and that of Galerkin method are indistinguishable.

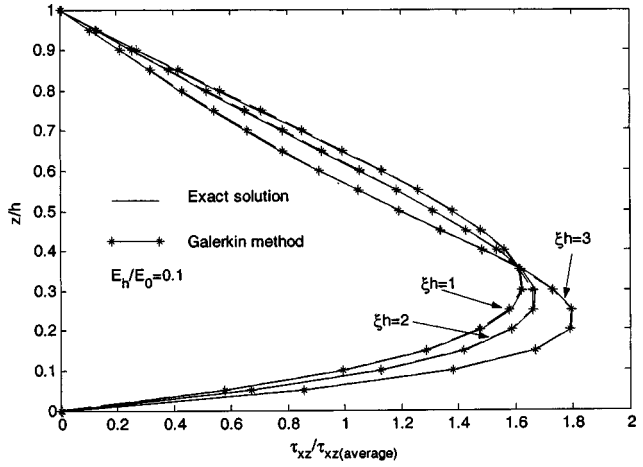

Fig. 5 Transverse shear stress through the thickness of FGM beam for $E_h = 0.1\,E_0$. The exact solution and that of Galerkin method are indistinguishable.

Acknowledgment

This research has been supported by the NASA Langley Research Center Grant NAG-1-1887. The authors are thankful to Dr. D. R. Ambur, Head, Mechanics & Durability Branch, for many suggestions and constant encouragement.

References

[1] Suresh, S., and Mortensen, A., 1998, *Fundamentals of Functionally Graded Materials*, IOM Communications Ltd., London.

[2] Pindera, M.-J., and Dunn, P., 1995, "An Evaluation of Coupled Microstructural Approach for the Analysis of Functionally Graded Composites via the Finite Element Method," NASA CR 195455, Lewis Research Center, Cleveland, OH.

[3] Delale, F., and Erdogan, F., 1983, "The Crack Problem for a Nonhomogeneous Plane," ASME J. Appl. Mech., **50**, pp. 609–614.

[4] Sankar, B. V., 2001, "An Elasticity Solution for Functionally Graded Beams," Compos. Sci. Technol., **61**, pp. 689–696.

[5] Sankar, B. V., and Tzeng, J. T., 2002, "Thermal Stresses in Functionally Graded Beams," AIAA J., **40**(6), pp. 1228–1232.

[6] Venkataraman, S., and Sankar, B. V., 2001, "Analysis of Sandwich Beams With Functionally Graded Core," AIAA Paper 2001-1281.

[7] Apetre, N. A., Sankar, B. V., and Venkataraman, S., 2002, "Indentation of a Sandwich Beam With Functionally Graded Core," AIAA Paper 2002-1683.

Fracture of Brittle Microbeams

M. Ostoja-Starzewski
Department of Mechanical Engineering, McGill University, 817 Sherbrooke Street West Montreal, PQ H3A 2K6, Canada
e-mail: martin.ostoja@mcgill.ca
Fellow ASME

The random polycrystalline microstructure of microbeams necessitates a reexamination of the crack driving force G stemming from the Griffith fracture criterion. It is found that, in the case of dead-load conditions, G computed by straightforward averaging of the spatially random elastic modulus E is lower than that obtained by correct ensemble averaging of the stored elastic energy. This result holds for both Euler-Bernoulli and Timoshenko models of micro-beams. However, under fixed-grip conditions G is to be computed by a direct ensemble averaging of E. It turns out that these two cases provide bounds on G under mixed loading. Furthermore, crack stability is shown to involve a stochastic competition between potential and surface energies, whose weak randomness leads to a relatively stronger randomness of the critical crack length. [DOI: 10.1115/1.1651091]

Background

According to Griffith's theory, [1], of elastic-brittle solids, the strain energy release rate G is given by

$$G=\frac{\partial W}{\partial A}-\frac{\partial U}{\partial A}=2\gamma \tag{1}$$

where A is the crack surface area formed, W is the work performed by the applied loads, U is the elastic strain energy, and γ is the energy required to form a unit of new material surface (e.g., [2]). The material parameter γ is conventionally taken as constant, but, given the presence of a randomly microheterogeneous material structure, its random field nature is sometimes considered explicitly (e.g., [3,4]). If one recognizes, however, that the random material structure also affects the elastic moduli, the computation of the left-hand side of (1) needs to be reexamined as well. Furthermore, randomness of both potential and surface energies will result in a stochastic, rather than deterministic, crack stability criterion. These issues are studied here in the case of cracking involving a beam-type configuration.

Dead-Load Conditions

This case of constant load implies that the force is nonrandom, but the kinematic variable is random. Now, only the second term in (1) remains, and, assuming an Euler-Bernoulli beam, the strain energy is

$$U(a)=\int_0^a \frac{M^2}{2IE}\,dx, \tag{2}$$

where a is crack length, M is bending moment, I is beam's moment of inertia, and E is elastic modulus. Henceforth, we simply work with $a=A/B$, where B is the constant beam (and crack) width. In view of Clapeyron's theorem, the strain energy release rate may be written as

$$G=\frac{\partial U}{B\partial a}. \tag{3}$$

Now, if the beam's material is random, E is a random field parametrized by x, which we can write as a sum of a constant mean $\langle E\rangle$ and a zero-mean fluctuation $E'(x)$

$$E(\omega,x)=\langle E\rangle+E'(\omega,x)\qquad \omega\in\Omega, \tag{4}$$

where Ω is a sample space. Take $E'(x,\omega)$ as a wide-sense stationary random field. A random material is thus defined as an ensemble $\mathcal{B}=\{B(\omega);\omega\in\Omega\}=\{E(\omega,x);\omega\in\Omega,x\in[0,a]\}$. Here, and in the following, we explicitly show the dependence on ω, whenever we wish to indicate the random nature of a given quantity prior to ensemble averaging.

On the physical side, the need to consider randomness of E arises when the representative volume element (RVE) of continuum mechanics cannot be safely applied to the actual beam. Among others, problems of this type are driven by the challenges of micro and nanotechnology; see, e.g., ([5,6]). Such a case is shown in Fig. 1, where a so-called *microbeam* is so thin that its lateral dimension L—i.e., the very one defining its Young's modulus—begins to be comparable to the crystal size d. The "comparable" aspect is described by a mesoscale L/d, and the RVE is to be replaced by a statistical volume element (SVE). The finite-size scaling laws of the SVE—i.e., its approach to the RVE with $L/d\to\infty$—were recently reviewed in [7].

It follows from (1) that U is a random integral, such that, for each and every realization $\omega\in\Omega$, we should consider

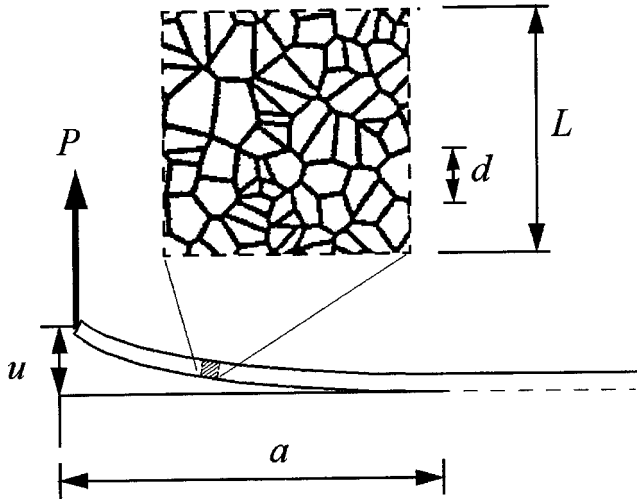

Fig. 1 Fracture of a microbeam of thickness *L* off a substrate. A statistical volume element (SVE) imposed by the random microheterogeneous structure characterized by scale *d* is shown.

Contributed by the Applied Mechanics Division of THE AMERICAN SOCIETY OF MECHANICAL ENGINEERS for publication in the ASME JOURNAL OF APPLIED MECHANICS. Manuscript received by the ASME Applied Mechanics Division, Dec. 16, 2002; final revision, Aug. 1, 2003. Associate Editor: M.-J. Pindera.

$$U(a,E(\omega))=\int_0^a \frac{M^2dx}{2IE(\omega,x)}. \tag{5}$$

Upon ensemble averaging, this leads to an average energy

$$\langle U(a,E)\rangle=\left\langle \int_0^a \frac{M^2dx}{2I[\langle E\rangle+E'(\omega,x)]}\right\rangle. \tag{6}$$

In the conventional formulation of deterministic fracture mechanics, random microscale heterogeneities $E'(x,\omega)$ are disregarded, and (5) is evaluated by simply replacing the denominator by $\langle E\rangle$, so that

$$U(a,\langle E\rangle)=\int_0^a \frac{M^2dx}{2I\langle E\rangle}. \tag{7}$$

Clearly, this amounts to postulating that the response of an idealized homogeneous material is equal to that of a random one on average. Therefore, we are interested in making a statement about $\langle U(a,E)\rangle$ versus $U(a,\langle E\rangle)$, and about $\langle G(E)\rangle$ versus $G(\langle E\rangle)$.

First, note that, since the random process E is positive-valued almost surely (i.e., with probability one), Jensen's inequality, [8], yields an inequality between harmonic and arithmetic averages of the random variable $E(\omega)$

$$\frac{1}{\langle E\rangle}\leqslant\left\langle\frac{1}{E}\right\rangle, \tag{8}$$

whereby the x-dependence is immaterial in view of the assumed wide-sense stationarity of field E. With (6) and (7), this implies that

$$U(a,\langle E\rangle)=\int_0^a \frac{M^2dx}{2I\langle E\rangle}\leqslant\int_0^a \frac{M^2}{2I}\left\langle\frac{1}{E}\right\rangle dx$$

$$=\left\langle \int_0^a \frac{M^2dx}{2IE(\omega,x)}\right\rangle=\langle U(a,E)\rangle, \tag{9}$$

since the conditions required by Fubini's theorem, [8] are met.

Now, if we define the strain energy release rate $G(a,\langle E\rangle)$ in a hypothetical material specified by $\langle E\rangle$, and the strain energy release rate $\langle G(a,E)\rangle$ properly ensemble averaged in the random material $\{E(\omega,x);\omega\in\Omega,x\in[0,a]\}$

$$G(a,\langle E\rangle)=\frac{\partial U(a,\langle E\rangle)}{B\partial a}\quad \langle G(a,E)\rangle=\frac{\partial\langle U(a,E)\rangle}{B\partial a}, \tag{10}$$

and note that the side condition is the same in both cases

$$U(a,\langle E\rangle)|_{a=0}=0\quad \langle U(a,E)\rangle|_{a=0}=0, \tag{11}$$

we obtain

$$G(a,\langle E\rangle)\leqslant\langle G(a,E)\rangle. \tag{12}$$

This provides a formula for the ensemble average G under dead-load conditions using deterministic fracture mechanics for Euler-Bernoulli beams made of random materials.

Another derivation of this is obtained by first introducing a complementary energy through an application of a *random Legendre transformation*, [9],

$$U^*(a,E(\omega))=M\cdot\theta-U(a,E(\omega))\quad \omega\in\Omega, \tag{13}$$

where θ is the angle of twist conjugate to M, such that

$$U^*(a,E(\omega))=\int_0^a \frac{IE(\omega)}{2}\theta^2dx. \tag{14}$$

It then follows from (8) that

$$U^*(a,\langle E(\omega)\rangle)=\int_0^a \frac{I\langle E(\omega)\rangle}{2}\theta^2dx\geqslant\int_0^a \frac{I\langle E^{-1}(\omega)\rangle^{-1}}{2}\theta^2dx$$

$$=U^*(a,\langle E^{-1}(\omega)\rangle^{-1}), \tag{15}$$

which, with the side condition

$$U^*(a,\langle E\rangle)|_{a=0}=0\quad U^*(a,\langle E^{-1}\rangle^{-1})|_{a=0}=0, \tag{16}$$

and the definitions

$$G^*(a,\langle E\rangle)=\frac{\partial U(a,\langle E\rangle)}{B\partial a}\quad G^*(a,\langle E^{-1}\rangle^{-1})=\frac{\partial U(a,\langle E^{-1}\rangle^{-1}}{B\partial a}, \tag{17}$$

yields

$$G^*(a,\langle E\rangle)\geqslant G^*(a,\langle E^{-1}\rangle^{-1}). \tag{18}$$

Since $G(a,\langle E\rangle)=G^*(a,\langle E\rangle)$ in a linear elastic material, we obtain (12).

Inequality (12) shows that G computed under the assumption that the random material is directly replaced by a homogeneous material ($E(x,\omega)=\langle E\rangle$), is lower than G computed with E taken explicitly as a spatially varying material property. Clearly, $\langle G(a,E)\rangle$ is the correct quantity to be used under dead loading.

Remark 1. With the beam thickness L increasing, the mesoscale L/d grows, so that $E'\to 0$. Thus, $\langle E^{-1}\rangle^{-1}\to\langle E\rangle$, and (12) turns into an equality, whereby the deterministic fracture mechanics is recovered.

Remark 2. These results carry over to a Timoshenko beam. In that case, strain energy is defined by

$$U(a)=\int_0^a \frac{M^2}{2IE}dx+\int_0^a \frac{V^2}{2A\mu}dx, \tag{19}$$

where V is shear force, A is beam's moment of inertia, and μ is shear modulus. The random material is now defined as a vector random field $\mathcal{B}=\{C(\omega,x);\omega\in\Omega,x\in[0,a]\}$, where the stiffness $C=[E,\mu]$. With the strain energy release rate defined by (3), we now derive

$$G(a,\langle E\rangle,\langle\mu\rangle)\leqslant\langle G(a,E,\mu)\rangle=G^*(a,\langle E^{-1}\rangle^{-1},\langle\mu^{-1}\rangle^{-1}). \tag{20}$$

The equality in (20) follows from the random Legendre transformation.

Fixed-Grip Conditions

In this case the displacement is constant (i.e., nonrandom), and the load is random. Now, only the first term in (1) remains so that

$$G=-\frac{\partial U^e(a)}{B\partial a}. \tag{21}$$

Suppose now that there is loading by a force P at the tip, so that we have

$$G=-\frac{u}{2B}\frac{\partial P}{\partial a}. \tag{22}$$

Take now a cantilever beam problem implying $P=3uEI/a^3$. Then, we find

$$\langle G\rangle=-\frac{u}{2B}\left\langle\frac{\partial P}{\partial a}\right\rangle=-\frac{u}{2B}\frac{\partial\langle P\rangle}{\partial a}=\frac{9u^2I\langle E\rangle}{2Ba^4}. \tag{23}$$

Since the load—be it a force and/or a moment—is always proportional to E, this indicates that G can be computed by a direct ensemble averaging of E under fixed-grip loading, and, indeed, the same conclusion carries over to Timoshenko beams.

Mixed-Loading Conditions

In general, both load and displacement vary during crack growth, and there is no explicit relation between the crack driving force and the change in elastic strain energy. However, we can bound G under mixed loading (G_{mixed}) by G under dead load (G_P) and G under fixed grip (G_u), providing we note the following facts:

(i) Observe that $G_P=\langle G(a,E)\rangle$, while $G_u=G(a,\langle E\rangle)$. Clearly, in view of (18), the ensemble averages satisfy

$$G_u \leqslant G_P . \tag{24}$$

(ii) Any (dP,du) change in the P, u-plane, corresponding to G_{mixed} due to an extension of the crack by da, may be split into two parts: $(0,du)$ and $(dP,0)$. The first part, involving an extension of the crack by $(da)_1$, is computed as $G_P=\langle G(a+(da)_1,E)\rangle$. The second part, involving an extension of the crack by $(da)_2$, is computed as $G_u=G(a+(da)_2,\langle E\rangle)$.

(iii) Observe that

$$G_{\text{mixed}}(a+da)=G_u(a+(da)_2)+G_P(a+(da)_1)\leqslant G_P(a+da) \tag{25}$$

because $G_u(a+(da)_2)\leqslant G_P(a+(da)_2)$ by (24), while

$$G_{\text{mixed}}(a+da)=G_u(a+(da)_1)+G_P(a+(da)_2)\geqslant G_u(a+da) \tag{26}$$

because $G_P(a+(da)_1)\geqslant G_u(a+(da)_1)$ again by (24).

It follows that G_{mixed} due to $da=(da)_1+(da)_2$ is bounded by the G's computed under dead-load and fixed-grip conditions, from above and below, respectively:

$$G_u \leqslant G_{\text{mixed}} \leqslant G_P . \tag{27}$$

Note that, interestingly, in mechanics of random media, the energy-type inequalites are usually ordered in an inverse fashion: kinematic (resp. force) conditions provide upper (resp. lower) bounds.

Moving on to the case of Timoshenko beam loaded at the tip, we have four particular possibilities:

(i) P and M fixed: G_{P-M},
(ii) P and θ fixed: $G_{P-\theta}$,
(iii) u and M fixed: G_{u-M},
(iv) u and θ fixed: $G_{u-\theta}$,

wherein $G_{P-\theta}$ and G_{u-M} are G's under mixed conditions. Now, in place of (24) we have

$$G_{u-\theta}\leqslant G_{P-\theta}\leqslant G_{P-M} \quad G_{u-\theta}\leqslant G_{u-M}\leqslant G_{P-M} . \tag{28}$$

Stochastic Crack Stability

Recalling the fracture criterion (1), we observe that cracking along the x axis is governed by an interplay of two random fields (parametrized by x): the elastic property E and the surface energy density γ. In view of the scaling arguments concerning the SVE versus the RVE in the paragraph following Eq. (4), the first one is a function of the beam thickness L, but the second one is not. Thus, for statistically stationary and ergodic materials, the randomness of E decreases to zero as the mesoscale $L/d\to\infty$, but the randomness of γ remains constant. To sum up, cracking of micro-beams is more sensitive to the material randomness of elastic moduli than cracking of, say, large plates.

Crack stability in any particular micro-beam ($\omega\in\Omega$), in a general loading situation, is governed by the condition of the same form as that in deterministic fracture mechanics, [2],

$$\frac{\partial^2(\Pi(\omega)+\Gamma(\omega))}{\partial a^2}\begin{cases}<0: & \text{unstable equilibrium}\\ =0: & \text{neutral equilibrium}\\ >0: & \text{stable equilibrium.}\end{cases} \tag{29}$$

Here both, the total potential energy $\Pi(\omega)$ and the surface energy $\Gamma(\omega)$ are random. Now, under dead-load conditions, the correctly averaged $\langle\Pi\rangle$ (shown by a solid line) is bounded from above by the deterministic Π estimated by a straightforward averaging of E

$$\Pi(\langle 1/E\rangle)=\langle\Pi\rangle\leqslant\Pi(\langle E\rangle). \tag{30}$$

The above follows again from (8). Typically, the energy Π goes like $-a^3$. Thus, in Fig. 2, we use a wedge of two parabolas to indicate scatter associated with the mean

$$\Pi(\langle 1/E\rangle)=\langle\Pi\rangle. \tag{31}$$

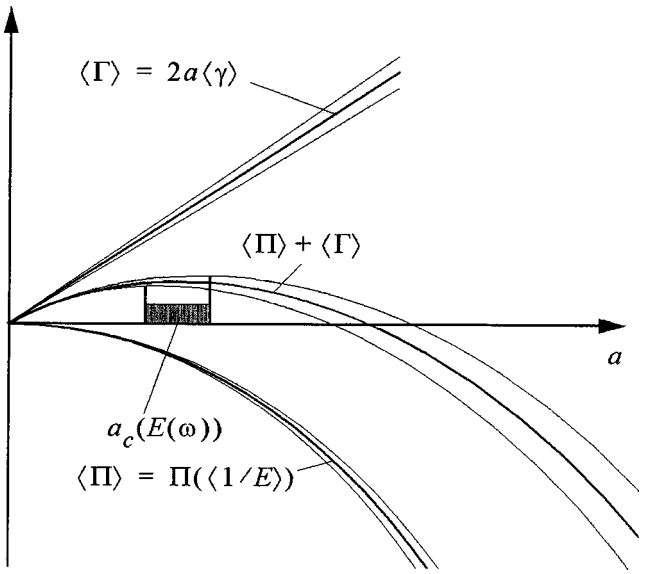

Fig. 2 Potential energy $\Pi(\langle 1/E\rangle)$ (thick line) and its scatter shown by a parabolic wedge (thin lines), summed with the surface energy $\langle\Gamma\rangle=2a\langle\gamma\rangle$ (thick line) and its scatter shown by a straight wedge (thin lines), results in $\Pi(\langle 1/E\rangle)+\langle\Gamma\rangle$ (thick line) and having scatter shown by a wider parabolic wedge (thin lines). Dashed region indicates the range of a critical crack length $a_c(E(\omega))$, a random variable.

Next, if we take, in analogy to (4), the surface energy density as a random field made up of a constant mean $\langle\gamma\rangle$ and a zero-mean fluctuation $\gamma'(x)$

$$\gamma(\omega,x)=\langle\gamma\rangle+\gamma'(\omega,x) \quad \omega\in\Omega, \tag{32}$$

then the surface energy $\Gamma(\omega)=2a[\langle\gamma\rangle+\gamma'(\omega)]$. Thus, using two straight lines, we indicate scatter about $\langle\Gamma\rangle=2a\langle\gamma\rangle$. Consequently, the scatter about the mean of $\Pi(\omega)+\Gamma(\omega)$ is larger than that of $\Pi(\omega)$ or $\Gamma(\omega)$ alone, and at the maximum of their sum we have a stochastic competition between both contributions. Evidently, according to (29), the critical crack length a_c becomes a random variable—i.e., $a_c(E(\omega))$—and we show its range by a dashed region in Fig. 2. In view of (30), there is an inequality between the average a_c properly calculated from $\Pi(\langle 1/E\rangle)$

$$\frac{\partial^2[\Pi(\langle 1/E\rangle)+\langle\Gamma\rangle]}{\partial a^2}=0\Rightarrow a_c(\langle 1/E\rangle)=\langle a_c(E)\rangle \tag{33}$$

and the deterministic a_c simplistically calculated from $\Pi(\langle E\rangle)$ is

$$\frac{\partial^2[\Pi(\langle E\rangle)+\langle\Gamma\rangle]}{\partial a^2}=0\Rightarrow a_c(\langle E\rangle). \tag{34}$$

The said inequality is

$$a_c(\langle 1/E\rangle)\leqslant a_c(\langle E\rangle). \tag{35}$$

Note that the equality $a_c(\langle 1/E\rangle)=\langle a_c(E)\rangle$ in (33) follows from (31). Finally, Fig. 2 shows that small random fluctuations in E and γ (i.e., scatter about the maximum of $\Pi(\langle 1/E\rangle)+\langle\Gamma\rangle$) lead to relatively much stronger (!) fluctuations in a_c.

Acknowledgment

Constructive comments of two anonymous reviewers helped in this work. The author also gratefully acknowledges the support of this research by the NSERC and the Canada Research Chairs Program.

References

[1] Griffith, A. A., 1921, "The Phenomena of Rupture and Flow in Solids," Philos. Trans. R. Soc. London, Ser. A, **221**, pp. 163–198.
[2] Gdoutos, E. E., 1993, *Fracture Mechanics: An Introduction*, Kluwer, Dordrecht, The Netherlands.
[3] Chudnovsky, A., and Kunin, B., 1987, "A Probabilistic Model of Brittle Crack Formation," J. Appl. Phys., **62**(10), pp. 4124–4129.
[4] Kunin, B., 1994, "A Stochastic Model for Slow Crack Growth in Brittle Materials," Appl. Mech. Rev., **47**, pp. 175–183.
[5] Altus, E., 2001, "Statistical Modeling of Heterogeneous Micro-Beams," Int. J. Solids Struct., **38**(34–35), pp. 5915–5934.
[6] Beran, M. J., 1998, "The Use of Classical Beam Theory for Micro-Beams Composed of Crystals," Int. J. Solids Struct., **35**(19), pp. 2407–2412.
[7] Ostoja-Starzewski, M., 2001, "Mechanics of Random Materials: Stochastics, Scale Effects, and Computation," *Mechanics of Random and Multiscale Microstructures*, D. Jeulin and M. Ostoja-Starzewski, eds., CISM Courses and Lectures **430**, Springer, Wien, pp. 93–161.
[8] Rudin, W., 1974, *Real and Complex Analysis*, McGraw-Hill, New York.
[9] Ostoja-Starzewski, M., 2002, "Microstructural Randomness Versus Representative Volume Element in Thermomechanics," ASME J. Appl. Mech., **69**, pp. 25–35.

Elastic-Plastic Stress Distribution in a Plastically Anisotropic Rotating Disk

N. Alexandrova
Department of Civil Engineering, University of Aveiro, 3810-193 Aveiro, Portugal
e-mail: nalexandrova@civil.ua.pt

S. Alexandrov
Institute for Problems in Mechanics, Russian Academy of Sciences, 101-1 Prospect Vernadskogo, 119526 Moscow, Russia
e-mail: sergei_alexandrov@yahoo.com

The plane state of stress in an elastic-plastic rotating anisotropic annular disk is studied. To incorporate the effect of anisotropy on the plastic flow, Hill's quadratic orthotropic yield criterion and its associated flow rule are adopted. A semi-analytical solution is obtained. The solution is illustrated by numerical calculations showing various aspects of the influence of plastic anisotropy on the stress distribution in the rotating disk.

[DOI: 10.1115/1.1751183]

1 Introduction

The dependence of stress distribution on the angular velocity in rotating disks is of significant importance due to a large number of applications. The majority of the work in this area is based on the assumption that the material is isotropic and obeys Tresca yield criterion with its associated flow rule (see [1] and a review in this paper). A comparison of the solutions for elastic-plastic rotating solid and annular disks based on Tresca and Mises yield criteria was given in [2]. In particular, the difference in stress distribution calculated with those two criteria was discussed. The effect of yield criteria on the stress distribution and limit angular velocity of a rotating disk with variable thickness was also investigated in [3]. In [4,5], the influence of temperature fields on the development of plastic zones in nonrotating thin disks was demonstrated. In particular, it appeared that the rise in temperature at which the entire plate became plastic was very small for various plate geometries. Summarizing the results obtained in [2–5] one may expect that deviations from isotropic material response can have a significant effect on the development of plastic zones in thin rotating disks. Elastic solutions for solid and annular rotating anisotropic disks were found in [6,7]. Plastic solutions for such disks are not available, to the best of our knowledge. Among the various theories of anisotropic plasticity, the one based on Hill's yield criterion and its associated flow rule, [8], is simplest and most popular. This yield criterion is adopted in the present paper. An axisymmetric problem is formulated assuming that the principal axes of anisotropy coincide with the radial and circumferential directions in plane of a thin disk rotating about its axis. The edges of the disk are stress free, and stresses are continuous across the elastic-plastic boundary. A semi-analytical solution is found under plane stress conditions.

Contributed by the Applied Mechanics Division of THE AMERICAN SOCIETY OF MECHANICAL ENGINEERS for publication in the ASME JOURNAL OF APPLIED MECHANICS. Manuscript received by the ASME Applied Mechanics Division, January 3, 2003, final revision, October 17, 2003. Associate Editor: M.-J. Pindera.

2 Solution

Consider a circular disk of outer radius b and inner radius a rotating with an angular velocity ω about its axis. The thickness of the disk is assumed to be small such that the plane state of stress can be adopted. In a cylindrical coordinate system $r\theta z$ with its z-axis coinciding with the axis of rotation, there are only two nonzero components of the stress tensor, σ_r and σ_θ. The elastic properties of the material are assumed to be isotropic, and the elastic portion of the strain tensor obeys Hooke's law. In the cylindrical coordinates chosen, Hill's yield criterion has the form

$$(G+H)\sigma_r^2-2H\sigma_r\sigma_\theta+(H+F)\sigma_\theta^2=1 \tag{1}$$

where G, H, F are constants which characterize the current state of material anisotropy. It is convenient to rewrite (1) as

$$\sigma_r^2+p_\theta^2-\eta\sigma_r p_\theta=\sigma_0^2 \tag{2}$$

where

$$\eta=2H/\sqrt{(G+H)(H+F)},\quad \eta_1=\sqrt{G+H}/\sqrt{H+F},$$
$$\sigma_0=1/(G+H),\quad p_\theta=\sigma_\theta/\eta_1. \tag{3}$$

The only nontrivial equation of motion is

$$\frac{\partial\sigma_r}{\partial r}+\frac{\sigma_r-\sigma_\theta}{r}=-\rho\omega^2 r, \tag{4}$$

where ρ the density of the material. The boundary conditions are

$$\sigma_r=0 \quad \text{at } r=a \quad \text{and} \quad r=b. \tag{5}$$

At small ω the entire disk is elastic. Since the elastic properties are assumed to be isotropic, the general solution for stresses is well known (see, for example, [9]). Using (5) the distribution of stresses can be found in the following form:

$$\sigma_r=\frac{3+\nu}{8}\rho\omega^2\left(a^2+b^2-\frac{a^2b^2}{r^2}-r^2\right),$$
$$\sigma_\theta=\frac{3+\nu}{8}\rho\omega^2\left(a^2+b^2+\frac{a^2b^2}{r^2}-\frac{1+3\nu}{3+\nu}r^2\right) \tag{6}$$

where ν is Poisson's ratio. Assume that yielding begins at the inner radius of the disk (it will be verified a posteriori). Then, using (3) and taking into account that $\sigma_\theta>0$, the angular velocity at the initial yielding, ω_e, is obtained by substitution of (6) into (2)

$$\frac{\rho\omega_e^2b^2}{\sigma_0}=\frac{4\eta_1}{(3+\nu)+(1-\nu)(a^2/b^2)}. \tag{7}$$

If ω is higher than ω_e, a plastic zone appears in the disk. The angular velocity at which the entire disk becomes plastic will be denoted by ω_p. In the range $\omega_e<\omega<\omega_p$ the disk consists of an inner plastic zone surrounded by an outer elastic zone. To find the distribution of stresses in the plastic zone, it is convenient to introduce the following nondimensional quantities:

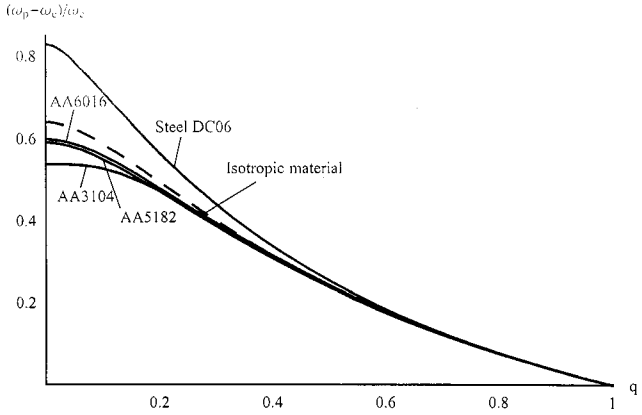

Fig. 1 Variation of the nondimensional quantity $(\omega_p-\omega_e)/\omega_e$ with q

$$\Omega=\rho\omega^2b^2/\sigma_0,\quad q=a/b,\quad \beta=r/b,\quad \gamma=c/b \tag{8}$$

where c is the radius of the elastic-plastic boundary. Equation (2) is satisfied automatically by the substitution

$$\sigma_r/\sigma_0=2\cos\varphi/\sqrt{4-\eta^2},\quad p_\theta/\sigma_0=\eta\cos\varphi/\sqrt{4-\eta^2}+\sin\varphi \tag{9}$$

where φ is a function of β. Substituting (9) into (4), with the use of (3), leads to the following ordinary differential equation for φ:

$$\frac{2\sin\varphi}{\sqrt{4-\eta^2}}\frac{d\varphi}{d\beta}-\left(\frac{2F\cos\varphi}{(H+F)\sqrt{4-\eta^2}}-\eta_1\sin\varphi\right)\frac{1}{\beta}-\Omega\beta=0. \tag{10}$$

The boundary condition to this equation follows from (5) at $r=a$ and (9) in the form

$$\varphi=\pi/2 \tag{11}$$

at $\beta=q$. The solution to (10) satisfying the boundary condition (11) can be obtained numerically and gives φ as a function of β. This function is not monotonic, φ attains its maximum at some value of β and, then, decreases. If the entire disk is plastic, then $\varphi=\pi/2$ at $\beta=1$, as follows from (5) at $r=b$ and (9). For a given value of q, it is clear from (10) that φ depends on β and Ω, $\varphi=\varphi(\beta,\Omega)$. Therefore, the solution to the equation $\varphi(1,\Omega_p)=\pi/2$, if it exists, gives the value of Ω_p corresponding to ω_p. The variation of the nondimensional quantity $(\omega_p-\omega_e)/\omega_e$ with q is shown in Fig. 1.

Once the solution to (10) has been found, the distribution of stresses in the plastic zone $q\leqslant\beta\leqslant\gamma$ is given by (9) with the use of (3). The general stress solution given in [9] is valid in the elastic region $\gamma\leqslant\beta\leqslant1$. Using the boundary condition (5) at $r=b$ and notation (8) it may be rewritten as

$$\frac{\sigma_r}{\sigma_0}=\frac{B}{\sigma_0}\left(\frac{1}{\beta^2}-1\right)+\frac{3+\nu}{8}\Omega(1-\beta^2),$$
$$\frac{\sigma_\theta}{\sigma_0}=-\frac{B}{\sigma_0}\left(\frac{1}{\beta^2}+1\right)+\frac{1+3\nu}{8}\Omega\left(\frac{3+\nu}{1+3\nu}-\beta^2\right) \tag{12}$$

where B is an arbitrary constant. For a given angular velocity in the range $\omega_e<\omega<\omega_p$ the magnitudes of γ and B can be determined from the condition of continuity of the stresses across the elastic-plastic boundary. At $\beta=\gamma$, it follows from (3), (9), and (12),

$$\frac{B}{\sigma_0}=\frac{1}{(1/\gamma^2-1)}\left[\frac{2}{\sqrt{4-\eta^2}}\cos\varphi_\gamma-\frac{3+\nu}{8}\Omega(1-\gamma^2)\right] \tag{13}$$

$$\frac{1}{4}[3+\nu+\gamma^2(1-\nu)]\Omega=\frac{\cos\varphi_\gamma}{\sqrt{4-\eta^2}}\left(\eta\eta_1+2\frac{1+\gamma^2}{1-\gamma^2}\right)+\eta_1\sin\varphi_\gamma \tag{14}$$

where φ_γ is the value of φ at $\beta=\gamma$ and is a function of γ since the solution to (10) gives φ as a function of β. Equation (14) should be solved numerically to obtain γ as a function of Ω. Then, B can be found as a function of Ω with the use of (13).

3 Numerical Results and Discussion

To illustrate the effect of plastic anisotropy on the development of the plastic zone some numerical results are presented in this section. In all cases, $\nu=1/3$. The solution for the isotropic material is obtained as a particular case of the general solution found at $F=G=H$. In Figs. 1–4, the corresponding calculations are illustrated by dashed lines. Four sets of anisotropic coefficients are considered ([10,11]):

$F/(G+H)=0.243$, $H/(G+H)=0.703$ for steel DC06;

$F/(G+H)=0.587$,

$H/(G+H)=0.410$ for aluminum alloy AA6016;

$F/(G+H)=0.498$,

$H/(G+H)=0.419$ for aluminum alloy AA5182;

$F/(G+H)=0.239$,

$H/(G+H)=0.301$ for aluminum alloy AA3104.

Note that the coefficients were measured for rolled sheets with straight principal axes of anisotropy. It is clear that the disk under consideration cannot be made of such sheets. However, for illus-

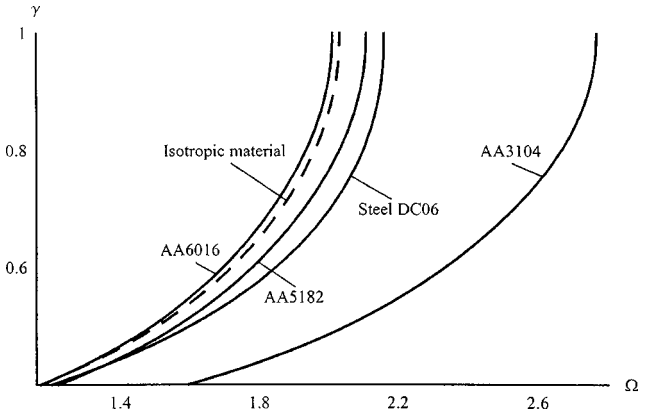

Fig. 2 Variation of the nondimensional radius of elastic-plastic boundary, γ, with Ω at $q=0.4$

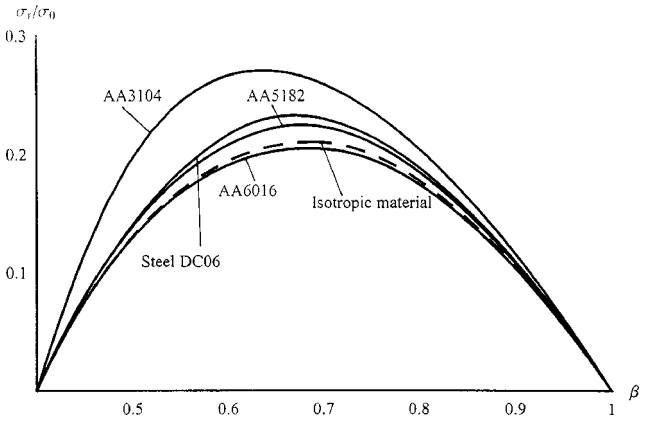

Fig. 3 Radial stress distribution at $\Omega=1.85$ and $q=0.4$

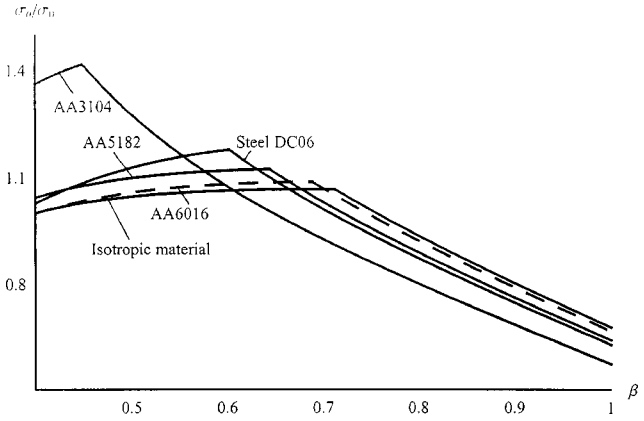

Fig. 4 Circumferential stress distribution at $\Omega=1.85$ and $q=0.4$

trative purposes it is possible to use the aforementioned coefficients for characterizing the level of anisotropy at each point. Figure 2 shows the variation of the radius of elastic-plastic boundary, γ, with Ω at $q=0.4$. Figures 3 and 4 illustrate typical radial and circumferential stress distributions at $\Omega=1.85$ and $q=0.4$, respectively.

There are two main conclusions to be made. First, the qualitative behavior of all curves is the same for anisotropic and isotropic materials: the increase in the angular velocity from ω_e to ω_p is relatively small (Fig. 1), and it tends to be smaller for the aluminum alloys of lower series. This is also illustrated in Fig. 2. Second, the anisotropic plastic properties have a significant effect on the size of the plastic zone and the stress distributions (Figs. 3 and 4). It is expected that this effect may have an influence on residual stress distributions, fatigue crack growth and other properties.

Acknowledgments

N.A. gratefully acknowledges support from the Foundation for Science and Technology (Portugal) under grant SFRH/BPD/6549/2001.

Nomenclature

a, b = inner and outer radii of the disk, respectively
c = elastic-plastic boundary
p_0 = modified tangential stress
q = ratio of the inner to outer radius of the disk
$r\theta z$ = cylindrical coordinate system
β = nondimensional polar radius
γ = nondimensional radius of the elastic-plastic boundary
η, η_1 = plastic anisotropic parameters
ν = Poisson's ratio
ρ = density of the material
σ_r, σ_θ = components of the stress tensor in the cylindrical coordinate system
φ = function of r
φ_γ = value of φ at $\beta=\gamma$
Ω = nondimensional parameter
ω = angular velocity
ω_e = angular velocity at the initial yielding
ω_p = angular velocity at which the entire disk becomes plastic

References

[1] Eraslan, A. N., and Orcan, Y., 2002, "Elastic-Plastic Deformation of a Rotating Solid Disk of Exponentially Varying Thickness," Mech. Mater., **34**, pp. 423–432.
[2] Rees, D. W. A., 1999, "Elastic-Plastic Stresses in Rotating Discs by von Mises and Tresca," Z. Angew. Math. Mech., **79**(4), pp. 281–288.
[3] Ma, G., Hao, H., and Miyamoto, Y., 2001, "Limit Angular Velocity of Rotating Disc With Unified Yield Criterion," Int. J. Mech. Sci., **43**, pp. 1137–1153.
[4] Alexandrov, S. E., and Chikanova, N. N., 2000, "Elastic-Plastic Stress-Strain State of a Plate With a Pressed-in Inclusion in Thermal Field," Mech. Solids, **35**(4), pp. 125–132.
[5] Alexandrov, S., and Alexandrova, N., 2001, "Thermal Effects on the Development of Plastic Zones in Thin Axisymmetric Plates," J. Strain Anal., **36**, pp. 169–176.
[6] Reddy, T. Y., and Srinath, H., 1974, "Elastic Stresses in a Rotating Anisotropic Annular Disk of Variable Thickness and Variable Density," Int. J. Mech. Sci., **16**, pp. 85–89.
[7] Zhou, F., and Ogawa, A., 2002, "Elastic Solutions for a Solid Rotating Disk With Cubic Anisotropy," ASME J. Appl. Mech., **69**, pp. 81–83.
[8] Hill, R., 1950, *Mathematical Theory of Plasticity*, Oxford University Press, London.
[9] Timoshenko, S. P., and Goodier, J. N., 1970, *Theory of Elasticity*, 3rd Ed., McGraw-Hill, New York.
[10] Bouvier, S., Teodosiu, C., Haddadi, H., and Tabacaru, V., 2002, "Anisotropic Work-Hardening Behavior of Structural Steels and Aluminium Alloys at Large Strains," *Proc. Sixth European Mechanics of Materials Conference*, S. Cescotto, ed., University of Liege-Belgium, EMAS, pp. 329–336.
[11] Wu, P. D., Jain, M., Savoie, J., MacEwen, S. R., Tugcu, P., and Neale, K. W., 2003, "Evaluation of Anisotropic Yield Functions for Aluminum Sheets," Int. J. Plasticity, **19**, pp. 121–138.

Saint-Venant Decay Rates for the Rectangular Cross Section Rod

N. G. Stephen
School of Engineering Sciences, Mechanical Engineering, The University of Southampton, Highfield, Southampton SO17 1BJ, UK

P. J. Wang
School of Mechanical, Materials, Manufacturing Engineering and Management, The University of Nottingham, University Park, Nottingham NG7 2RD, UK

A finite element-transfer matrix procedure developed for determination of Saint-Venant decay rates of self-equilibrated loading at one end of a semi-infinite prismatic elastic rod of general cross section, which are the eigenvalues of a single repeating cell transfer matrix, is applied to the case of a rectangular cross section. First, a characteristic length of the rod is modelled within a finite element code; a superelement stiffness matrix relating force and displacement components at the master nodes at the ends of the length is then constructed, and its manipulation provides the transfer matrix, from which the eigenvalues and eigenvectors are determined. Over the range from plane stress to plane strain, which are the extremes of aspect ratio, there are always eigenmodes which decay slower than the generalized Papkovitch-Fadle modes, the latter being largely insensitive to aspect ratio. For compact cross sections, close to square, the slowest decay is for a mode having a distribution of axial displacement reminiscent of that associated with warping during torsion; for less compact cross sections, slowest decay is for a mode characterized by cross-sectional bending, caused by self-equilibrated twisting moment.

[DOI: 10.1115/1.1687794]

1 Introduction

For a one-dimensional, beam-like structure, Saint-Venant's principle (SVP) allows one to replace a known load system on one end by a statically equivalent load distributed in a particular way demanded by the elastostatic solution, known as the relaxed end

Contributed by the Applied Mechanics Division of THE AMERICAN SOCIETY OF MECHANICAL ENGINEERS for publication in the ASME JOURNAL OF APPLIED MECHANICS. Manuscript received by the ASME Applied Mechanics Division, Jan. 22, 2003; final revision, Oct. 28, 2003. Associate Editor: K. R. Rajagopal.

condition. Statically equivalent implies that the resultant force and moment are unchanged; the difference between the two load distributions is termed self-equilibrating and since it has no resultant force or couple that requires reaction at some other locations on the structure, there is no reason why the associated stress and strain field should penetrate any great distance into the structure. That is the self-equilibrating load should produce only a local effect, which decays as one moves away from the beam end. On the other hand, more often than not, the exact distribution is not known, only the magnitude of the end load; either way, SVP is rarely invoked consciously, yet it underpins the day-to-day application of the discipline of strength of materials.

Exact elasticity solutions for these end effects are available when the rod has a mathematically amenable boundary, such as the solid and hollow circular cross section, [1,2]; however, for the important case of a rod of rectangular cross section, the well-known Papkovitch-Fadle (P-F) modes (see, for example, [3]), apply only to the extremes of aspect ratio which are plane strain and plane stress, and are subject to their inherent stress and displacement assumptions, while an antiplane solution, [4], assumes infinite width.

Toupin [5] provided the first proof of SVP in 1965, and there has been extensive research since that time, with reviews having been provided by Horgan and Knowles, [6–8]. Toupin argued that attempts to calculate decay rates are not ''*consistent with the spirit of the principle, and the way it is used. After all, if one can construct, or is willing to construct solutions, there is no need for the principle.*'' A counter view is that a knowledge of the minimum decay rate for a particular structure defines the extent of the region where a calculated stress may be in error. In a recent paper, [9], the present authors described a numerical procedure which allowed the determination of the Saint-Venant decay rates for a semi-infinite elastic rod of arbitrary cross section subjected to self-equilibrated loading at one end. This procedure is, in turn, a development of a transfer matrix method, [10], in which the decay rates and equivalent continuum beam properties of a repetitive pin-jointed framework, consisting of a series of identical cells, can be calculated. Nodal displacements and forces on either side of the generic cell form state vectors which are related by means of a transfer matrix, the latter being determined from a knowledge of the cell stiffness matrix; on account of translational symmetry, consecutive state vectors are related by a constant multiple λ, the decay factor, which leads directly to a standard eigenvalue problem. For the continuum elastic beam of arbitrary cross section, the beam is first regarded as a series of identical cells of a characteristic length, related to some cross-sectional dimension; the stiffness matrix of one such cell is constructed using a finite element code, such as ANSYS. Since displacement and force components are required only for master nodes at the ends of the cell, all others are treated as slave nodes. This condensation creates a superelement stiffness matrix, which is imported into a MATLAB environment where the manipulations to form the transfer matrix and determination of the eigenvalues are readily accomplished. Accuracy of the method was established in [9] by comparison with the decay rate predictions from a selection of the stock of exact elasticity solutions, and found to be excellent. The theory behind the method was described fully in [9], and is not repeated here.

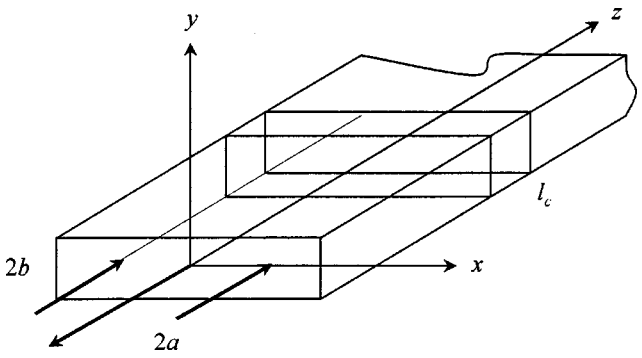

Fig. 1 Semi-infinite elastic rod of rectangular cross section subject to self-equilibrated load on the end $z=0$, and repeating cell of length l_c

2 Finite Element Modelling of the Cell

Figure 1 shows a typical repeating cell of the rod having width $2a$, depth $2b$ and length l_c. For numerical purposes we take b and l_c as equal to unity, when the calculated decay rates, over the range of aspect ratios $a/b=1/20\rightarrow 40$, are a multiple of the rod semi-depth b. The modelling data are given in Table 1; in all cases 20-node isoperimetric elements were used and Poisson's ratio was taken to be 0.25. The large dimension of the transfer matrix, for example 576×576 in the case of the square cross section, in turn leads to a large number of possible decay modes; 12 of the eigenvalues are equal to unity and these pertain to the six rigid body displacements, and the six transmission modes of tension, torsion, and shear and bending in two planes. The remaining eigenvalues occur as reciprocal pairs (the transfer matrix being symplectic) according to whether decay is from left to right, or vice versa, which leads to the prediction of 282 distinct left to right decay modes. Of these, the most important (and the most accurate) are those which provide the slowest (spatially) rates of decay; thus for the square cross section, only the first ten decay rates are presented, allowing some classification into families of decay modes.

Table 1 Finite element modeling data of rectangular crosssection of characteristic length, l_c

Aspect ratio a/b	Division of $2a\times2b$	Division of length, l_c	Number of elements	Nodes in cross-section	Size of transer matrix
1/20	4×8	10	320	121	726×726
1/10	4×8	10	320	121	726×726
1/4	3×8	5	120	95	570×570
1/2	3×8	5	120	95	570×570
2/3	4×6	5	120	93	558×558
4/5	4×6	5	120	93	558×558
1	5×5	5	125	96	576×576
5/4	6×4	5	120	93	558×558
3/2	6×4	5	120	93	558×558
2	8×3	5	120	95	570×570
4	8×3	5	120	95	570×570
10	8×4	5	160	121	726×726
20	8×4	5	160	121	726×726
40	8×4	5	160	121	726×726

Table 2 Slowest decay rates (kb) for various aspect ratios a/b. Shaded entries are those closest to the plane stress/strain Papkovitch-Fadle (P-F) and antiplane shear modes.

Aspect Ratio a/b	1/20	1/10	1/4	1/2	2/3	4/5	1	5/4	3/2	2	4	10	20	40
Exact	1.2985	1.3424	1.4996	1.7999	2.0420	1.8672± 0.6101*i*	1.6639± 0.5717*i*	1.4938± 0.4881*i*	1.3613	0.9000	0.3749	0.1345	0.0648	0.0319
2.1061± 1.1254*i*	2.1065± 1.1256*i*	2.1066± 1.1257*i*	2.1069± 1.1258*i*	2.1077± 1.1295*i*	2.0602± 0.5897*i*	2.0959± 1.1513*i*	1.9917± 1.1546*i*	1.6767± 0.9210*i*	1.3735± 0.3932*i*	1.0538± 0.5648*i*	0.5267± 0.2815*i*	0.2107± 0.1126*i*	0.1053± 0.0563*i*	0.0527± 0.0281*i*
	2.2884± 0.0534*i*	2.1514	2.1207	2.3902± 0.3650*i*	2.1060± 1.1386*i*	2.2734	2.2391± 1.1072*i*	1.8188	1.4040± 0.7591*i*	1.1951± 0.1826*i*	0.5302	0.2154	0.1146± 0.0022*i*	0.0573± 0.0031*i*
3.7488± 1.3843*i*	3.7538± 1.3848*i*	2.5242	2.8533	3.5074± 1.0764*i*	3.1086± 0.9965*i*	2.6663± 1.3941*i*	2.5474± 0.9238*i*	2.1330± 1.1154*i*	2.0723± 0.6645*i*	1.7535± 0.5385*i*	0.7133	0.2523	0.1877± 0.0692*i*	0.0938± 0.0346*i*
	3.9203± 0.6011*i*	3.7535± 1.3849*i*	3.7568± 1.3851*i*	3.7660± 1.4250*i*	3.1825± 1.6861*i*	2.8570± 0.9283*i*	2.5474± 0.9238*i*	2.2855± 0.7427*i*	2.1216± 1.1243*i*	1.8826± 0.7128*i*	0.9390± 0.3464*i*	0.3754± 0.1385*i*	0.1968± 0.0301*i*	0.0986± 0.0159*i*
5.3563± 1.5516*i*	5.3843± 1.5475*i*	4.0050± 0.5656*i*	4.1868± 0.6795*i*	3.9704	3.3620± 1.5510*i*	2.9431± 1.2492*i*	2.6221	2.3545± 0.9996*i*	2.2412± 1.0343*i*	1.9856	1.0468± 0.1701*i*	0.3997± 0.0567*i*	0.2693± 0.0773*i*	0.1346± 0.0387*i*
	5.6001± 0.9056*i*	5.3853± 1.5467*i*	5.3926± 1.5473*i*	4.2459± 2.2807*i*	3.8533± 1.3859*i*	3.1661	2.6672± 1.0872*i*	2.5329	2.5692± 0.9242*i*	2.1238± 1.1439*i*	1.3486± 0.3874*i*	0.5386± 0.1546*i*	↓	↓
6.9500± 1.6761*i*	7.0457± 1.6458*i*	5.6602± 0.8421*i*	5.7122± 1.2234*i*	4.4496± 2.1304*i*	3.8786	3.4276	2.6882	2.7421	2.5858	2.2264± 1.0688*i*	1.4284± 0.3071*i*	↓	↓	↓
$\pi/2 = 1.5708$		7.0696± 1.6502*i*	6.5369	4.7288± 1.3045*i*	4.0178	3.7984± 1.3745*i*	3.7970± 1.3876*i*	3.0389± 1.0999*i*	2.6787	2.3636± 0.6534*i*	1.6368	1.5795	1.5735	1.5718
					4.3477± 1.2607*i*		3.7970± 1.3876*i*	↓	↓	↓	↓	↓	↓	↓
								3.8331± 1.4297*i*	3.8309± 1.4160*i*	3.7496± 1.6404*i*	2.1239± 1.1439*i*	2.1133± 1.1293*i*	2.1133± 1.1304*i*	2.1130± 1.1308*i*
								4.0006± 1.3390*i*	3.9427± 1.3754*i*	3.8124± 1.6022*i*	2.1488± 1.1244*i*	2.1188± 1.1249*i*	2.1150± 1.1289*i*	2.1136± 1.1305*i*
											↓	↓	↓	↓
											3.7481± 1.6425*i*	3.8378± 1.4283*i*	3.8374± 1.4297*i*	3.8370± 1.4298*i*
											3.7655± 1.6320*i*	3.8412± 1.4255*i*	3.8392± 1.4295*i*	3.8376± 1.4302*i*

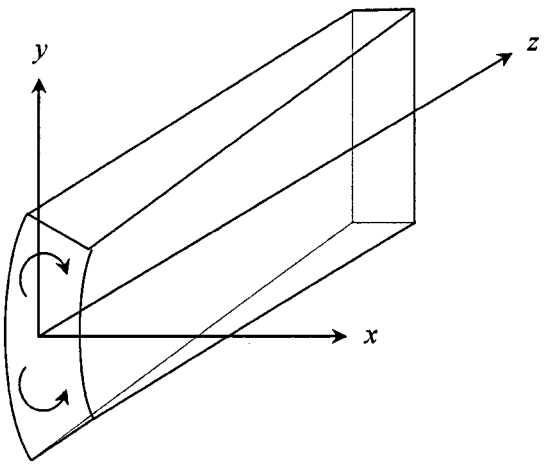

Fig. 2 Self-equilibrated twisting moment on the end $z=0$; aspect ratio $a/b<1$

3 Results and Discussion

The slowest decay rate predictions are shown in Table 2, in ascending magnitude of the real part which governs the rate of decay; thus the first row pertains to self-equilibrated loading that will penetrate the greatest distance into the structure. Exact decay rates are available only at the extremes of aspect ratio, for generalized plane stress ($a/b\rightarrow 0$) and plane strain ($a/b\rightarrow\infty$) when stress decays exponentially from one end as $\exp(-kz)$, where k are the roots of the well-known Papkovitch-Fadle (P-F) eigenequation (see [3], article 26)

$$\sin 2kb \pm 2kb = 0; \tag{1}$$

the two smallest roots are $kb=2.1062\pm 1.1254i$, $kb=5.3563\pm 1.5516i$ for the positive sign in Eq. (1), which is the symmetric case, and $kb=3.7488\pm 1.3843i$, $kb=6.9500\pm 1.6761i$ for the negative sign, the asymmetric case. In the case of antiplane strain, [4], decay from the loaded edge is as $\exp(-n\pi z/2b)$, where n is an integer, implying a slowest decay given by the root $kb=\pi/2$; these exact decay rates are shown in the first column The shaded entries in Table 2 are those that, by virtue of similarity of the displacement field, are closest to these known exact solutions, and are here regarded as generalized P-F or generalized shear modes.

First, it is noted that the decay rates of the generalized P-F modes appear largely insensitive to aspect ratio; thus for the cases $a/b\leqslant 2/3$, the real part of the slowest generalized symmetric P-F mode exceeds that of the exact plane stress value (2.1062) by less than 0.1%, and for $a/b=4/5$ it is less than the plane stress value by 0.5%. The maximum deviation occurs for the square cross section, $a/b=1$, at less than +7%. For the slowest asymmetric generalized P-F mode, the real part exceeds the plane stress value (3.7488) by less than 3% for $a/b\leqslant 1$.

For all aspect ratios considered, there is at least one mode that decays slower than the generalized P-F modes. For $a/b\leqslant 1$, the mode associated with the real root is characterized by a bending of the cross section due to self-equilibrated twisting moment in the xy-plane, as depicted in Fig. 2. The mode associated with the complex root is characterized by an axial warping displacement field reminiscent of Saint-Venant torsion, and hence a stress field associated with the restraint of torsional warping (here referred to as the bi-moment mode).

For the cases $a/b>5/4$, Table 2, there are an increasing number of modes which decay slower than the slowest P-F modes; again the smallest of these modes is characterized by cross-sectional bending, but in fact they are physically the same modes of decay as those which provide the smallest decay rates for $a/b<4/5$; thus consider the dual relationship between the decay rates for the two cases $a/b=2/3$ and $a/b=3/2$; physically the bars are identical, the difference being an interchange of the coordinate axes and, by implication, the dimensions a and b. The slowest decay rate for $a/b=2/3$ is $kb=2.0420$, when stress decays as $\exp(-2.0420z/b)=\exp(-1.3613z/a)$, which is the smallest decay rate for $a/b=3/2$, albeit with a and b reversed; generalization of this result is straightforward for other aspect ratios. For any particular aspect ratio $a/b<1$, a dual decay rate may be found by simply multiplying by the aspect ratio: thus an entry for $a/b=4$ can be found from the decay rate for $a/b=1/4$, and multiplying by 1/4; for example, $1.4996\times 1/4=0.3749$. Indeed, in Table 2, with the exception of those entries below the symbol $\downarrow$, which denotes that some decay rates have not been entered, every decay mode for $a/b<1$ has a dual for $a/b>1$ on the same row.

Compared to the general rectangle, which is symmetric about the coordinate axes, the square cross section is, in addition, symmetric about the two diagonals; in turn the decay rates can occur as single eigenvalues, or as pairs, according to the (a)symmetry of the displacement field. For the slowest bi-moment mode ($kb=1.6639\pm 0.5717i$) both the axial displacement, w, and the cross-sectional displacements, u and v, are symmetric with respect to the diagonals, and asymmetric with respect to the x and y-axes; in consequence a single root, and a single eigenvector (decay mode), suffices. On the other hand, repeated decay rates occur for symmetric cross-sectional bending ($2.5474\pm 0.9238i$) and the asymmetric P-F mode ($3.7970\pm 1.3876i$), but not for the asymmetric cross-sectional bending, or symmetric P-F modes. The single roots at $a/b=1$ show (a)symmetries, as follows:

$(1.6639\pm 0.5717i)$	u, v and w are symmetric about both diagonals, asymmetric about both coordinate axes
$(3.8804\pm 1.3623i)$	u, v and w are asymmetric about both diagonals and coordinate axes
4.0408	u, v and w are asymmetric about both diagonals and coordinate axes
$(2.2391\pm 1.1072i)$	u, v and w are symmetric about both diagonals and coordinate axes
$(1.9917\pm 1.1546i)$	u, v and w are symmetric about both coordinate axes, asymmetric about the diagonals

In each case, there are (a)symmetries for each of the three displacement components.

In contrast the modes pertaining to the double roots show a less developed pattern of (a)symmetry; for example,

$(2.5474\pm 0.9238i)$	one mode has u and v symmetric about the y-axis, asymmetric about the x-axis, no (a)symmetries about diagonal; w no (a)symmetries; the other mode has w symmetric about the x-axis, asymmetric about the y-axis, no (a)symmetries about diagonals; u and v show no (a)symmetries
$3.7970\pm 1.3876i$	one mode has w symmetric about one diagonal, asymmetric about the other; u and v show no (a)symmetries; the other mode has u and v asymmetric about the x-axis, symmetric about the y-axis; w shows no (a)symmetries.

Now there is planar (a)symmetry in respect of u and v, or (a)symmetries for the axial displacement w, but not both. Thus it appears that the occurrence, or otherwise, of a double decay mode depends on the degree of (a)symmetry in the displacement field.

Finally, we note in Table 2 a decay rate which approaches the slowest antiplane strain shear decay rate of $kb=\pi/2$, with an error of less than 0.6% when $a/b \geqslant 10$.

4 Concluding Remarks

For the rectangular cross section, there are always eigenmodes that decay slower than the Papkovitch-Fadle (P-F) modes; typically these are modes characterized by a bending of the cross section, which would be precluded by plane stress/plane strain assumptions. The exception is for a compact cross section, that is, close to being square, when slowest decay is for a mode associated with a bi-moment. However, the P-F modes remain important as a means of classification of the various decay modes.

In discussing the decay rates, attention has focused on the slowest, as it is these which validate Saint-Venant's principle; for the square cross section, the slowest Saint-Venant decay is as $\exp(-1.6639z/b)=\exp(-4.7062z/d)$ where $d=2\sqrt{2}b$ is the section diagonal, which is the greatest linear dimension of the cross-section; this implies that stress level reduces to less than 1% of free end value at distance $z=d$ from the free end, indicating that SVP is clearly applicable. On the other hand, at first sight a very small decay rate, such as $kb=0.0648$ for aspect ratio $a/b=20$, Table 2, might suggest that SVP is inapplicable; indeed the stress level only reduces to 87.8% of its free end value at distance $z=2b$ (that is, distance 1×plate thickness) from the free end. However, if the decay characteristic is expressed in terms of multiples of the diagonal $d=2\sqrt{401}b$, decay is as $\exp(-2.5952z/d)$. This implies stress reduction to less than 7.5% at distance $z=d$ from the free end, and to less than 0.6% at twice that distance; thus SVP is still clearly applicable so long as the decay characteristic and, more importantly, the sense in which SVP is understood, is in terms of multiples of the cross section greatest linear dimension which is dominated by plate width $2a$ for this aspect ratio.

Nomenclature

a, b = semi-width and semi-depth of rectangular cross section
d = greatest linear dimension of cross section ($d=2\sqrt{a^2+b^2}$)
i = $(-1)^{1/2}$
k = decay rate ($k=\ln\lambda$)
l_c = characteristic length
u, v, w = displacement components in the x, y, and z-directions
x, y, z = Cartesian coordinates
λ = decay factor, eigenvalue of transfer matrix

References

[1] Klemm, R. L., and Little, R. W., 1970, "The Semi-Infinite Elastic Cylinder Under Self-Equilibrated End Loading," SIAM (Soc. Ind. Appl. Math.) J. Appl. Math., **19**, pp. 712–719.
[2] Stephen, N. G., and Wang, M. Z., 1992, "Decay Rates for the Hollow Circular Cylinder," ASME J. Appl. Mech., **59**, pp. 747–753.
[3] Timoshenko, S. P., and Goodier, J. N., 1970, *Theory of Elasticity*, Third Ed., McGraw-Hill, New York, Art. 26.
[4] Shun, Cheng, 1979, "Elasticity Theory of Plates and a Refined Theory," ASME J. Appl. Mech., **46**, pp. 644–650.
[5] Toupin, R. A., 1965, "Saint-Venant's Principle," Arch. Ration. Mech. Anal., **18**, pp. 83–96.
[6] Horgan, C. O., and Knowles, J. K., 1983, "Recent Developments Concerning Saint-Venant's Principle," Adv. Appl. Mech., **23**, pp. 179–269.
[7] Horgan, C. O., 1989, "Recent Developments Concerning Saint-Venant's Principle: An Update," Appl. Mech. Rev., **42**, pp. 295–303.
[8] Horgan, C. O., 1996, "Recent Developments Concerning Saint-Venant's Principle: A Second Update," Appl. Mech. Rev., **49**, pp. 101–111.
[9] Stephen, N. G., and Wang, P. J., 1996, "Saint-Venant Decay Rates: A Procedure for the Prism of General Cross-Section," Comput. Struct., **58**, pp. 1059–1066.
[10] Stephen, N. G., and Wang, P. J., 1996, "On Saint-Venant's Principle for the Pin-Jointed Framework," Int. J. Solids Struct., **33**, pp. 79–97.

On Source-Limited Dislocations in Nanoindentation

M. X. Shi
Department of Theoretical and Applied Mechanics,
University of Illinois at Urbana-Champaign,
Urbana, IL 61801

Y. Huang[1]
Department of Mechanical and Industrial Engineering,
University of Illinois at Urbana-Champaign,
Urbana, IL 61801
e-mail: huang9@uiuc.edu

M. Li
Alcoa Technical Center, Alcoa Center, PA 15069

K. C. Hwang
Department of Engineering Mechanics,
Tsinghua University, Beijing 100084, P.R. China

The discrete dislocation model is used in this note to investigate the source-limited dislocation generation and glide in nanoindentation. It is shown that once there are enough sources for dislocation generation, the material behavior becomes independent of the dislocation source distribution. [DOI: 10.1115/1.1751185]

1 Introduction

Nanoindentation has become a major experimental technique to probe the mechanical properties of materials at the nanoscale, [1,2]. Dislocation glide underneath the nanoindenter is identified as the key mechanism of plastic deformation in nanoindentation, [3,4]. Dislocation loops are observed near the edge of the nanoindenter, [4]. The quasi-continuum analysis, [5], shows that dislocations are indeed generated right underneath the corner of the rectangular indenter and then moved into the bulk material. In this note we present a discrete dislocation analysis to investigate the effect of dislocation source distribution in nanoindentation, particularly the source-limited dislocation generation and glide (i.e., very few sources for dislocation generation). Following Shi et al. [6], we modify the two-dimensional discrete dislocation model of van der Giessen, Needleman and co-workers, [7,8], for the equilibrium dislocation analysis by requiring that the glide component of the Peach-Koehler force on each dislocation vanishes at each time step.

2 Equilibrium Analysis of Discrete Dislocations

We study a region of 4 μm×2 μm subject to pressure on the top surface over a zone of 0.8 μm. The Young's modulus is 70 GPa, and Poisson's ratio is 0.33. Figure 1 shows the symmetric, right-half region (2 μm×2 μm). The symmetry or traction-free conditions give that the shear stress tractions vanish on all boundaries. In addition, the left boundary is subject to the symmetry condition $u_x=0$. The right surface is traction free, so is the top surface except over the loading region where the pressure is applied (over the region of 0.4 μm). Here for simplicity we use the

[1]Two whom correspondence should be addressed.

Contributed by the Applied Mechanics Division of THE AMERICAN SOCIETY OF MECHANICAL ENGINEERS for publication in the ASME JOURNAL OF APPLIED MECHANICS. Manuscript received by the ASME Applied Mechanics Division, Aug. 12, 2002; final revision, Oct. 25, 2003. Associate Editor: T. E. Triantifyllides.

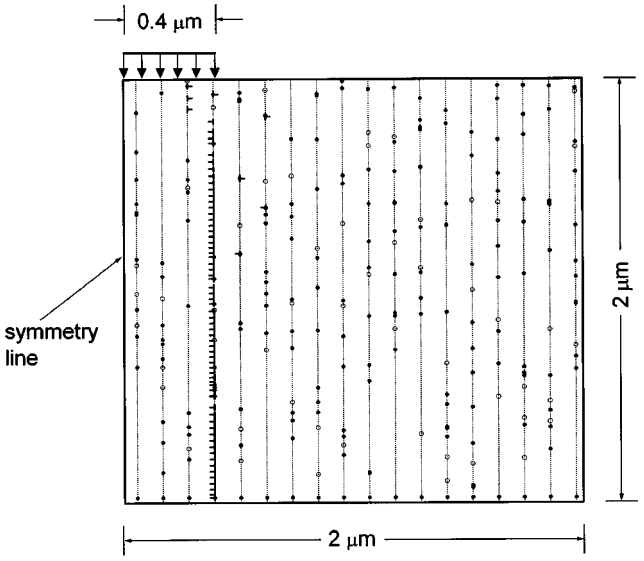

Fig. 1 Random distribution of dislocation sources (open circles) and obstacles (solid circles) on slip planes (dashed lines). There are 18 slip planes in the 2 μm×2 μm region, with 3 dislocation sources and 11 obstacles on each slip plane. The pressure is applied over a region of 0.4 μm on the top surface.

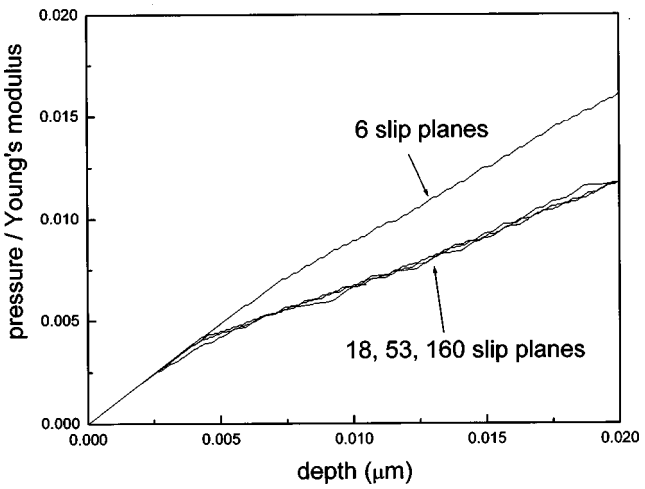

Fig. 2 The applied pressure (normalized by the Young's modulus) versus the indentation depth for the 2 μm×2 μm region in Fig. 1 with 6, 18, 53, and 160 slip planes

pressure in the finite loading region (0.4 μm) to represent the indentation. The bottom surface is also subject to boundary condition $u_y = 0$.

The right-half region in Fig. 1 contains 18 slip planes with the slip plane spacing 112.5 nm. We have chosen the slip planes parallel to the direction of pressure (on the top surface) since these slip planes allow dislocations to move downward, which is consistent with that observed by Tadmor et al. [5]. Initially, the solid is assumed to be free of mobile dislocations, but to contain a random distribution of dislocation sources and point obstacles. The sources mimic Frank-Read sources and generate a dislocation dipole when the Peach-Koehler force exceeds a critical value, [6–8]. The obstacles, which could be small precipitates or forest of dislocations, pin dislocations and will release them once the Peach-Koehler force attains the obstacle strength, [6–8].

There are three sources for dislocation generation (marked by open circles) randomly distributed on each slip plane, and their strength follows a normal distribution with the mean strength $\overline{\tau}_{\mathrm{NUC}} = 50$ MPa and standard deviation $0.2\overline{\tau}_{\mathrm{NUC}} = 10$ MPa. Once the glide component of the Peach-Koehler force exceeds $\tau_{\mathrm{NUC}} b$ over time $t_{\mathrm{NUC}} = 0.01$ μs, a dislocation dipole is generated, [6–8]. Here $b = 0.25$ nm is the length of the Burgers vector, and the glide component of the Peach-Koehler force on the Kth dislocation is given by

$$f^K = \mathbf{n}^{\mathbf{K}} \cdot \sigma \cdot \mathbf{b}^{\mathbf{K}}, \tag{1}$$

where $\mathbf{n}^{\mathbf{K}}$ is the slip plane normal, $\mathbf{b}^{\mathbf{K}}$ is the Burgers vector of the Kth dislocation and σ is the stress field excluding the contribution from the Kth dislocation itself.

There are ten obstacles (marked by solid circles) randomly distributed on each slip plane, with the obstacle strength $\tau_{\mathrm{OBS}} = 150$ MPa. When a dislocation meets an obstacle, it is pinned to this obstacle until the glide component of the Peach-Koehler force given in (1) exceeds $\tau_{\mathrm{OBS}} b$. On each slip plane there is an additional obstacle very close to the bottom surface with very large obstacle strength in order to prevent dislocations from exiting the bottom surface. This represents (or mimics) the effect of a hard substrate that blocks dislocations at the film/substrate interface. Dislocation annihilation is also accounted for. Two dislocations with opposite Burgers vectors on the same slip plane annihilate when their spacing is less than $6b$.

The same approach of van der Giessen, Needleman, and coworkers, [7,8], is used to decompose the problem into (1) an analytic solution for dislocations in an infinite solid, and (2) a finite element solution for a dislocation-free solid with finite boundaries. The finite element method can handle the second problem very effectively since it does not involve any singularities, [7,8]. However, Our analysis is different in that all dislocations reach equilibrium within each time increment, though they may exit the solid (from the top surface), or be pinned at obstacles. The dislocation positions are solved iteratively within each time increment until the glide component of the Peach-Koehler force vanishes for every dislocation, [6].

3 Results

Figure 1 also shows the dislocation distribution on all 18 slip planes in the solid at the pressure $0.012E$, where E is the Young's modulus. The distance between the end of loading region and the nearest slip plane is 6.25 nm. It is clearly observed that most dislocations are generated on the slip plane closest to the end of loading region. This is due to the high stress concentration at the end of loading region, [9]. In fact, the normal stress in the direction perpendicular to the applied pressure is even singular at the end of loading region, [9]. The pattern of dislocation distribution shown in Fig. 1 is similar to the patterns observed in the quasicontinuum analysis, [5], and experiments, [3,4].

In order to examine the effect of dislocation source distribution in nanoindentation, we have also studied the same region (2 μm×2 μm) with 6, 53, and 160 slip planes. The slip plane spacings are 337.5 nm, 37.5 nm, and 12.5 nm, respectively. The size of loading region remains the same (0.4 μm). The number of dislocation sources and obstacles also remain the same on each slip plane (3 and 10, respectively), but the total number of dislocation sources and obstacles for 6, 53, and 160 slip planes are approximately 1/3, 3, and 9 times of those shown in Fig. 1 for 18 slip planes. The distance between the end of loading region and the nearest slip plane is 106.25 nm for the solid with 6 slip planes, and this distance becomes 6.25 nm for 18, 53, and 160 slip planes. Figure 2 shows the applied pressure normalized by the Young's modulus versus the indentation depth for above four sets of slip planes, where the indentation depth is the maximum normal displacement (under the pressure) at the symmetry line. It is clearly observed that the curves for 18, 53, and 160 slip planes are essen-

tially the same, but the curve for 6 slip planes shows a much stiffer material response. The latter is therefore called the source-limited dislocation generation.

4 Concluding Remarks

The present note shows that, for source-limited dislocation generation (e.g., 6 slip planes with 18 dislocation sources), the material may display a stiff response. Once there are enough dislocation sources (e.g., 18, 53, or 160 slip planes with 54, 159, and 480 dislocation sources, respectively), the overall plastic response of the solid becomes independent of the dislocation source distribution. The present model oversimplifies dislocation activities (e.g., two-dimensional analysis, one set of slip planes, dislocation sources), but the above conclusion on source-limited dislocations in nanoindentation should hold qualitatively.

Acknowledgments

Y. H. acknowledges the support from NSF through grants 0084980 and 0103257, and NSFC. K. C. H. acknowledges the support from the Ministry of Education and NSFC.

References

[1] Nix, W. D., 1997, ''Elastic and Plastic Properties of Thin Films on Substrates: Nanoindentation Techniques,'' Mater. Sci. Eng., A, **234**, pp. 37–44.
[2] Gouldstone, A., Koh, H.-J., Zeng, K.-Y., Giannakopoulos, A. E., and Suresh, S., 2000, ''Discrete and Continuous Deformation During Nanoindentation of Thin Films,'' Acta Mater., **48**, pp. 2277–2295.
[3] Zielinski, W., Huang, H., Venkataraman, S., and Gerberich, W. W., 1995, ''Dislocation Distribution Under a Microindentation Into an Iron-Silicon Single Crystal,'' Philos. Mag. A, **72**, pp. 1221–1237.
[4] Gerberich, W. W., Nelson, J. C., Lilleodden, E. T., Anderson, P., and Wyrobek, J. T., 1996, ''Indentation Induced Dislocation Nucleation: The Initial Yield Point,'' Acta Mater., **44**, pp. 3585–3598.
[5] Tadmor, E. B., Miller, R., and Phillips, R., 1999, ''Nanoindentation and Incipient Plasticity,'' J. Mater. Res., **14**, pp. 2233–2250.
[6] Shi, M., Huang, Y., and Gao, H., 2003, ''The J-Integral and Geometrically Necessary Dislocations in Nonuniform Plastic Deformation,'' Int. J. Plasticity, in press.
[7] Needleman, A., and van der Giessen, E., 2001, ''Discrete Dislocation and Continuum Descriptions of Plastic Flow,'' Mater. Sci. Eng., A, **309**, pp. 1–13.
[8] van der Giessen, E., Deshpande, V. S., Cleveringa, H. H. M., and Needleman, A., 2001, ''Discrete Dislocation Plasticity and Crack Tip Fields in Single Crystals,'' J. Mech. Phys. Solids, **49**, pp. 2133–2153.
[9] Hills, D. A., and Nowell, D., 1994, *Mechanics of Fretting Fatigure*, Kluwer Academic Publishers, Boston.